



Mechanical Behavior and Fracture Evolution Mechanism of Composite Rock Under Triaxial Compression: Insights from Three-Dimensional DEM Modeling

Yu Song¹ · Sheng-Qi Yang¹ · Ke-Sheng Li¹ · Peng-Fei Yin¹ · Peng-Zhi Pan²

Received: 6 January 2023 / Accepted: 23 June 2023 / Published online: 21 July 2023
© The Author(s), under exclusive licence to Springer-Verlag GmbH Austria, part of Springer Nature 2023

Abstract

Existing studies on transversely isotropic rock formations, a special geology, have mainly focused on its mechanical characteristics; whereas, investigations on its fracture process and damage microscopic mechanisms are relatively limited. To remedy this deficiency, in this study, a three-dimensional numerical model is established using discrete elements (PFC^{3D}), focusing on the effects of confining pressure (0, 5, 10, 15, and 20 MPa) and laminar inclination angle (θ_{0° , θ_{15° , θ_{30° , θ_{45° , θ_{60° , θ_{75° , and θ_{90°) on the failure behavior of the composite rock. To demonstrate the accuracy of the simulations, the stress–strain curves and ultimate failure modes obtained from the numerical simulations were compared with the previous laboratory mechanical test results and X-ray CT images. Numerical models using the smooth-joint contact model were shown to simulate the laboratory results reasonably well. Numerical simulation results indicate that the confining pressure and laminar angle significantly influence the internal crack evolution patterns of the specimen. The internal cracks change from a concentrated to a discrete distribution as the confining pressure increases. The internal cracks of specimens with θ_{0° and θ_{90° laminar inclination emerges from the soft rock and eventually extends to the hard rock, while the inclined specimens crack from the laminar face and finally spread to the rock matrix, which can be explained by the graph of the increasing number of cracks. In addition, the internal principal stress and tangential stress in soft and hard rocks were monitored by arranging measurement circles, and it was found that the tangential stresses are the essential cause of the difference between the mechanical behavior of the two rock types.

Highlights

- The complicated three-dimensional discrete element transversely models captured the prospective mechanical behavior and cracking characteristic
- The failure patterns and crack coalescence process are characterized by various confining pressure and bedding inclination angles
- The difference behavior between the soft and hard rock matrix is dependent on the confining pressure and internal tangential stress

✉ Sheng-Qi Yang
yangsqi@hotmail.com

¹ State Key Laboratory for Geomechanics and Deep Underground Engineering, School of Mechanics and Civil Engineering, China University of Mining and Technology, Xuzhou 221116, People's Republic of China

² State Key Laboratory of Geomechanics and Geotechnical Engineering, The Chinese Academy of Sciences, Wuhan 430071, People's Republic of China

Keywords Transversely isotropic rock · Three-dimensional discrete element model · Weak bedding faces · Mechanical behavior · Fracture characteristics · Internal stress behavior

1 Introduction

Anisotropic rocks are often encountered in geotechnical engineering, and transversely isotropic rocks are among the most typical, mainly in sedimentary and metamorphic rocks. Challenges faced by geotechnical engineering with transversely isotropic layered rock mass range from study for feasibility of roller cutter excavation and stability of surrounding rock in mining and tunneling, exploration of the stability of large stratified slopes, foundation safety studies for large-scale facilities (hydroelectric power stations, nuclear waste plants, military bases) in bedded rock formations to the study of energy extraction issues such as shale gas, natural gas, and petroleum. Complex failure modes in different rock strata and the changes of deformation, strength, and permeability of anisotropic rock mass with various laminar tendencies arise due to the characteristics of directional dependency and the presence of multiple weak laminae.

In the past decades, lithology with inherently anisotropic structures was studied in meticulous detail; at the same time, the composite rock-like specimen characterized by conveniently available, mechanical equivalent, and reproducible was proposed for laboratory experimental investigation (Tien and Tsao 2000). On the one hand, hydrofracturing has become the main approach to address the problem of extracting shale gas stored in layered rocks; therefore, numerous Brazilian splitting tests were carried out to investigate the tensile strength of transversely isotropic shale (Cho et al. 2012; Vervoort et al. 2014; Roy and Singh 2015; Wang et al. 2016; Yang et al. 2019a and Yang et al. 2020). On the other hand, a considerable number of uniaxial and triaxial compression tests on transversely isotropic rocks had been carried out since the in situ rock is mostly in compression (Cho et al. 2012; Cheng et al. 2017, 2018, 2020; Yin and Yang 2018; Sapari and Zabidi 2019; Yang et al. 2019b; Ademović and Kurtović, 2021; Shen et al. 2021; Chen et al. 2022; He et al. 2022; Weng et al. 2022). Additionally, oblique shear test as well as three-point bending tests of transversely isotropic rocks were conducted to analyze the shear behavior and cracking toughness (Valente et al. 2012; Ghazvinian et al. 2013). In general, the main research content of these indoor experiments ranges from analysis of mineral composition, basic mechanical parameters, failure modes, crack types to the surface deformation. A variety of auxiliary methods are combined with these tests, such as acoustic emission localization (Cho et al. 2012; Wang et al. 2016; Cheng et al. 2017; Yang et al. 2019a, b), strain gauges (Roy and Singh 2015; Yang et al. 2019a), 3D digital image correlation system

(Cheng et al. 2017; Yin and Yang 2018; Yang et al. 2019b, 2020), and X-ray micro-CT observation (Yang et al. 2019b). However, most of these capabilities are limited to the surface of the specimen that cannot reflect the internal conditions of strain and stress and cracking characteristics (with the exception of X-ray micro-CT observation), and focus on the post-damage properties of the specimen rather than the real damage process. According to Duveau, the theoretical part of transversely isotropic rocks can be divided into three categories (Cao and Liu 2022), the first of which is called the mathematical continuum method, which treats anisotropic rocks as a whole irrespective of the action of weak surfaces and applies mathematical methods to describe their mechanical properties (Hill 1950; Tsai and Wu 1971; Deng et al. 2022). The second is an empirical formula commonly used in various fields, simply described as a formula to describe the interaction of loading direction with strength and deformation based on the results of numerous tests on anisotropic rocks (Saeidi et al. 2013, 2014; Singh et al. 2015). The last method deduces the intrinsic equations by considering the effect of discontinuous weak surfaces on anisotropic rocks individually (Shi et al. 2016; Liu et al. 2021; Wang et al. 2022; Dobróka et al. 2022), the most classical of which is the Jaeger's criterion derived on the basis of the More–Coulomb criterion (Jaeger 1960). In addition, the cross-sectional anisotropic rock ontogenetic equations for formations with different mechanical properties have become a hot topic in the last decade.

In recent years, discrete element numerical simulation has developed rapidly in the field of rocks due to its ability to simulate the process of rock damage and to verify the relevant theories, particularly with the particle flow code (PFC). Compared with the finite element simulation method, the discrete element method is not constrained by deformation and can effectively simulate the process of microscopic crack generation and expansion of the rock materials, and may be more applicable to transversely isotropic rock masses. In 2004, Potyondy et al. simulated rocks with dense interconnections of particles for the first time and successfully restored a wide range of rock properties, together with the sensitivity of particle microscopic parameters to macroscopic properties (Dong et al. 2022; Potyondy 2012). Subsequently granular flow code has gained unprecedented momentum in the rock sector (Potyondy and Cundall 2004; Potyondy 2015). With the contact model, extensive rock-like models are in the spotlight; Jiang et al. (2011) built a cement sand model by two-dimensional distinct element technology, and mechanical properties and strain localization of cement sand were investigated. Then, Lee and Jeon

(2011) proposed a novel method of cutting two unparallel fissures in rectangular model by PFC^{2D} to analyze the peak strength, ultimate failure mode, and crack initial stress compared to the experimental results of Hwangdeung granite. At the same time, Ivars et al. (2011) raised a new approach for analyzing the mechanical behavior of jointed rock mass by modeling the rock matrix with bonded particle model and representing the weak joint network with smooth-joint contact model (SJM). In this way, we can obtain properties that are not available through empirical modeling such as scale effect, anisotropy, permeability in multiple directions, and brittleness of complex rock masses. Then, Park and Min (2015) extended this approach to the study of transverse anisotropic rocks; the smooth-joint contact model was inserted in two-dimensional disk-shaped specimens for Brazilian tensile strength test and cylindrical specimens for uniaxial compressive strength test; the elastic and strength anisotropy of transversely isotropic rock model were researched compared with the laboratory experiment. In this way, He and Afolagboye (2018) and Yang et al. (2019a) investigated the mechanical behavior of shale with two-dimensional models based on the indoor tests of Brazilian splitting, and the crack coalescence process and failure modes are presented; four types of micro-cracks were classified to reveal the failure mechanism of the specimens by Yang. Additionally, Duan et al. (2016, Duan and Kwok 2016) applied this method into the issue of stress-induced borehole breakouts with a large-scale model in PFC^{2D}; the stress measurement and crack propagation around the borehole were discussed. Under complex stress conditions, Yin et al. (2019) investigated the composite rock-like specimen with two different layers through PFC^{2D}, the results were in good agreement with the laboratory tests. Sun et al. (2022) studied the bedded shale under two different unloading paths by 2D discrete element simulation, and the main focus is on the damage process of rock with energy dissipation, maximum principal stress field and microcrack evolution. Moreover, Chiu et al. (2013) and Mehranpour and Kulatilake (2017) each proposed their own improved smooth-joint models to research the anisotropic behavior of rock mass.

However, the results described above are limited to two-dimensional numerical simulations, which hardly reflect the mechanical properties of real rocks and unable extended to larger-scale models that can fit for the engineering. Therefore, 3D modeling has become a hot topic of research in the current years; Park et al. (2018) first attempted to simulate the triaxial tests of transversely isotropic rock by three-dimensional bonded discrete element modeling, but only the basic mechanical behavior and failure modes were analyzed. Meanwhile, Zhang et al. (2019) employed the SJM in 3D rectangular-shaped models to obtain the deformation and failure behavior

of anisotropic rock; the spatial distribution and directions of inner cracks were discussed; the results showed that the cracking pattern dominated from tensile cracks to shear cracks with increasing confining pressure. So far, very few research has been done on 3D modeling of transversely isotropic rocks, especially on 3D triaxial compression simulations of standard composite rock specimens.

Therefore, a three-dimensional procedure for generating the transversely isotropic composite rock-like specimens is presented in this paper. Then, the micro-parameters of parallel bonded contact and smooth-joint contact were calibrated based on the results of laboratory experiments completed by Yang et al. (2019b). Simulation of triaxial compressive tests of composite rock-like specimens with seven various inclinations were conducted. Subsequently, the internal crack propagation process as well as the damage mode and failure mechanism of the 3D composite rock model were analyzed compared with a series of X-ray CT images, while the characteristics of the principal stresses and shear stresses in the soft and hard rock formations during compression were discussed to reveal the cracking mechanism from weak material to robust material.

2 Three-Dimensional Numerical Simulation Methodologies

2.1 Brief Description of Laboratory Test

The composite rock-like material was fabricated by pouring layer by layer in prepared stiff plastic molds, where the rock layer with relatively weak mechanical properties is composed of ordinary Portland cement, water, gypsum, kaolinite powder, and fine quartz sand (1:0.75:0.15:0.3:1.2); conversely, sulfate aluminum cement, water, quartz sand, and iron powder (1:0.355:0.9:0.1) were used to fabricate the hard rock layer. In consideration of reflecting the cross-sectional isotropic properties of the composite rock and preventing excessive bedding effects that may lead to failure to represent the difference in mechanical properties between soft and hard rocks. Thus, the thickness of each layer was set to 10 cm in this study. The composite rock-like specimens from θ_{0° to θ_{90° were then obtained by drilling the artificial rock block in different directions with a 50 mm drill bit, and finally made into 50 × 100 mm standard cylindrical specimens. Figure 1 shows the drilling process. The physic and mechanical properties of composite rock-like material were obtained from cylinder specimens in the

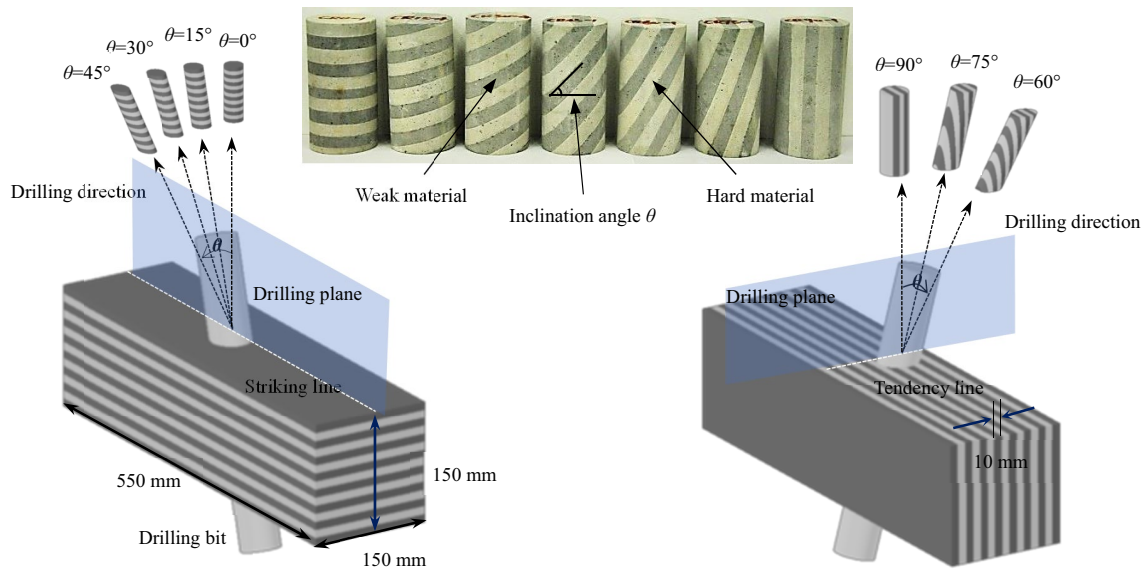


Fig. 1 Diagram of the drilling process for composite rock specimens with bedding angles from θ_0° to θ_{90° (Yang et al. 2019b)

Table 1 Macro-parameters obtained from the laboratory test (Yang et al. 2019b)

Material type	σ_c (MPa)	E_s (GPa)	μ	c (MPa)	φ ($^\circ$)	ρ (kg/m ³)
Weak	16.44	3.60	0.23	5.21	24	1627
Hard	68.43	23.69	0.34	18.17	40	1912

σ_c —compressive stress; E_s —Elastic modulus; μ —poisson' s ratio; c —cohesion; φ —friction angle; ρ —density

laboratory (Yang et al. 2019b), and the density, uniaxial compression strength, Young' s modulus, Poisson' s ratio of soft and hard rock was 1627 kg/m³, 16.44 MPa, 3.60 GPa, 0.23 and 1912 kg/m³, 68.43 MPa, 23.69 GPa, and 0.34, respectively (shown in Table 1).

2.2 Three-Dimensional Discrete Element Modeling

The challenge of using discrete elements to simulate composite rock materials involves two main aspects. One is how to distinguish soft and hard rocks and simulate their respective mechanical properties; the second point is how to simulate the behavioral characteristics of the contact at the interface of soft and hard material. Therefore, the selection of the correct contact model is crucial for the subsequent simulation. The simulations in this paper were performed in PFC3D 5.0 version, benefit from previous research, the synthetic rock mass (SRM, which generate synthetic rock masses using different contact models in PFC^{3D}) approach was followed. To demonstrate the lithology of the simulated rock-like matrix, this method uses parallel-bond model (PBM) to simulate soft and hard rock materials (Ivas and Pierce, 2011). Despite the fact that the Pb model does not characterize the exact compression–tension ratio compared

with the flat-joint model, it is advantageous to use the Pb model to study rock materials with high homogeneity from the results of statistical analysis as well as damage patterns. Therefore, the Pb model is more applicable due to the high homogeneity of the rock-like materials studied in this paper. Then, several joint surfaces were created by importing equal quantity circular plane of discrete fracture network (DFN, a DFN is the collection of a series of fractures). Eventually, the smooth joint bond is created before the DFN are deleted. In contrast to empirical methods of property estimation, the SRM method can obtain predictions of scale effects, anisotropy and crack evolution pattern at key locations of the rock mass. In addition, the impact of particle radius on the mechanical properties of the model can be ignored when the ratio of the minimum boundary to the maximum particle radius of the model is greater than 30 (Ding et al. 2014), and for consideration of the calculation speed, the number of particles was set to 30325 in this work.

The bonding behavior and rheological composition of the PBM as well as the SJM have been plotted in Fig. 2. The linear parallel bond model consists of a linear interface as well as a parallel bond interface (see Fig. 2b). When a parallel bond is bonded, it can withstand bending moments and its failure is controlled by the Coulomb criterion, which is

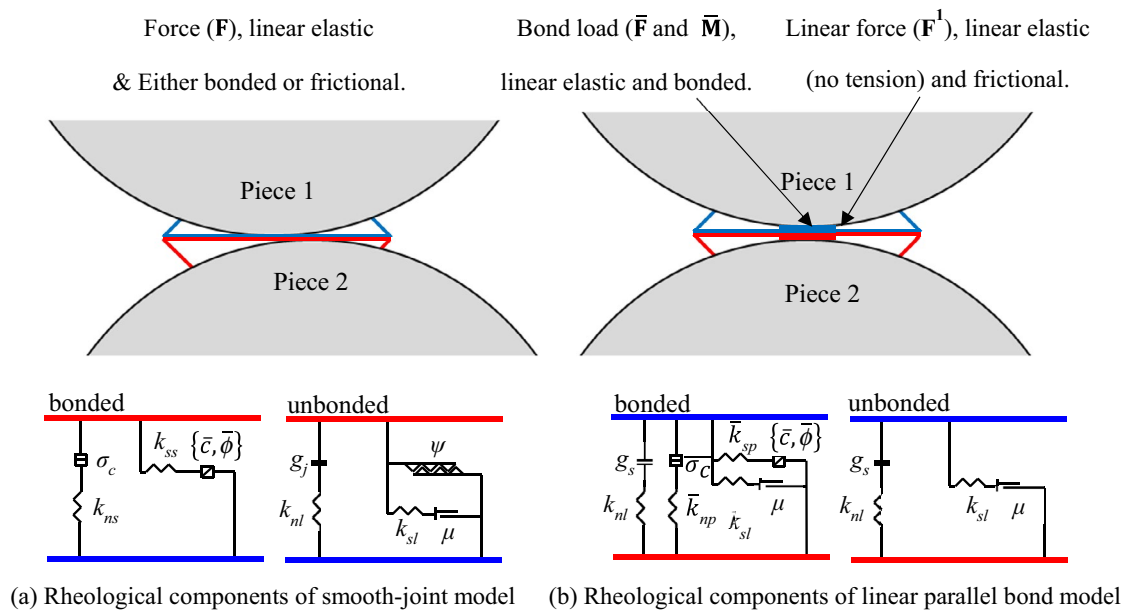


Fig. 2 Schematic diagram of bonding shape and rheological components of SJM and PBM

transformed into a linear model after fracture. The smooth joint model delivers the macroscopic behavior of a bonded or frictional interface that is linearly elastic and expansive (see Fig. 2a). The behavior of the bonded interface is linearly elastic until the strength limit is exceeded and the bond breaks, causing the interface to be unbonded, the behavior of the unbonded interface is linearly elastic and frictionally expansive, fitting the slip by imposing a Coulomb limit on the shear force. While, the interface does not resist relative rotation. It is worth noting that the stiffness in both components is independent of the particle diameters. Then, the particle model consisting of these two models with the inclination from θ_{0° to θ_{90° is presented in Fig. 3a, and the particle bond situation of both the weak and hard material is plotted in Fig. 3b. Finally, the contact model of composite rock-like with dip of θ_{45° is shown in Fig. 3c.

2.3 Confirmation for Micro-parameters

It is recommended that the jointed weak face of the soft and hard rock in the test composite specimen is of generally no thickness and does not bear pressure along the strike; however, the actual thickness of the jointed model in the numerical simulation exists and the pressure bearing on the strike gradually increases as the inclination of the weak face increases, resulting in non-negligible differences in the mechanical behavior of the composite rock model and the real rock-like specimen.

Considering the above problem, four categories of micro-parameters are calibrated: ball parameters (density; the maximum and minimum radius of the ball); linear-bond

parameters (the effective modulus; ratio of normal to shear stiffness); parallel-bond parameters (friction coefficient; friction angle; effective modulus; tensile strength; cohesion; and ratio of normal to shear stiffness); and smooth-joint parameters (friction coefficient; tensile strength; cohesion; normal stiffness; and shear stiffness). At the same time, the tensile strength of the PB model was deliberately reduced to make the compression–tension ratio of the model specimen consistent with that of the real rock. The trial-and-error method (fixing other parameters first, change only one parameter, and then change the next parameter after reaching the desired goal) was adopted to calibrate the parallel-bond parameters for uniaxial compression and compression with confining of the complete soft rock model and the complete hard rock model, respectively.

The elastic and strength parameters of smooth joint models are calibrated during two stages. We selected two special specimens at θ_{0° and θ_{45° to calibrate the parameters of smooth joint models, where the effect of the weak layer is small and almost negligible because the axial stress is perpendicular to the weak layer of the θ_{0° specimen, however, in the θ_{45° specimen, the weak layer plays a dominant role. In the first stage, we first fix the elastic parameters of parallel-bond model and set large values for the local strength parameters of the parallel bond and smooth joint models so that no failure of contacts occurs and its effect on elastic response is eliminated. Then, we adjust the normal stiffness k_n and tangential stiffness k_s by trial-and-error method until the macroscopic modulus of elasticity of θ_{0° specimens and θ_{45° specimens agreed with the test results. In the second stage, the elastic parameters identified during

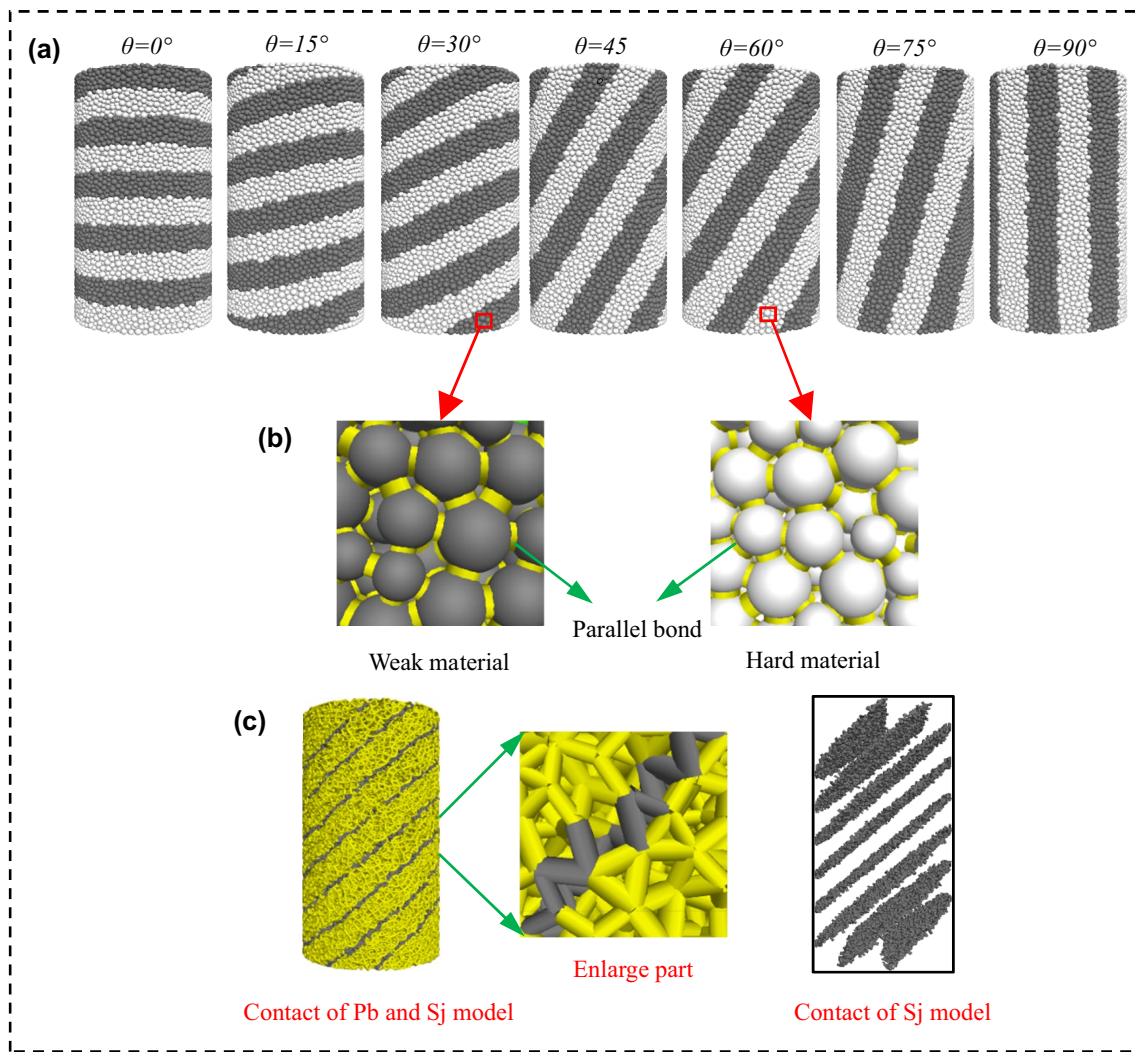


Fig. 3 Modeling of composite specimens. **a** particle models with the bedding angle from θ_{0° to θ_{90° ; **b** parallel bond of weak and hard material in the composite specimen of θ_{45° ; **c** contact of rock matrix and bedding surface

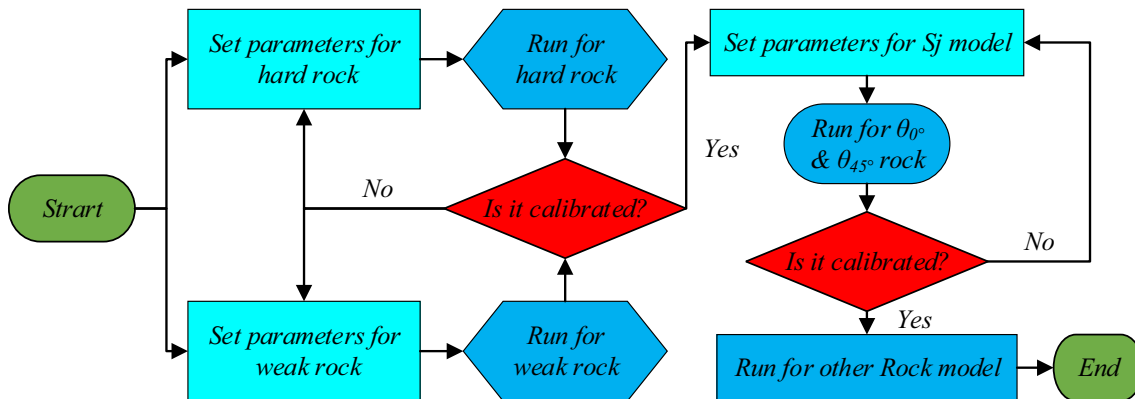


Fig. 4 Flowchart of the calibration process

Table 2 Micro-parameters of parallel-bond model and smooth-joint model to simulate the composite rock-like material

Parameter	Value		Parameter	Value	
	Material A	Material B		Material A	Material B
ρ (kg/m ³)	1627	1912	$Pb-E_c$ (GPa)	2.04	12
R_{min} (mm)	0.75	0.75	$Pb-ten$ (MPa)	2.67	11.8
R_{rat}	1.66	1.66	$Pb-coh$ (MPa)	26.7	118
$Lb-Ec$ (GPa)	2.04	12	$Sj-kn$ (GPa)	1500	1500
k_n/k_s	2.0	2.0	$Sj-ks$ (GPa)	1500	1500
$\bar{k}_n/\bar{k}_s k_n/k_s$	2.0	2.0	$Sj-ten$ (MPa)	5	5
$Pb-\mu$	0.5	0.5	$Sj-coh$ (MPa)	10	10
$Pb-\varphi$ (°)	24	40	$Sj-\mu$	0.5	0.5

R_{min} —the minimum radius of the ball; R_{rat} —ratio of the maximum to the minimum radius of the ball; $Lb-E_c$ —the effective modulus of linear bond; k_n/k_s —ratio of normal to shear stiffness of the linear bond; $\bar{k}_n/\bar{k}_s k_n/k_s$ —ratio of normal to shear stiffness of the linear parallel bond; $Pb-\mu$ —linear parallel-bond friction coefficient; $Pb-\varphi$ —friction angle of linear parallel bond; $Pb-E_c$ —effective modulus of linear parallel bond; $Pb-ten$ —tensile strength of linear parallel bond; $Pb-coh$ —cohesion of linear parallel bond; $Sj-kn$ —normal stiffness of smooth joint; $Sj-ks$ —shear stiffness of smooth joint; $Sj-ten$ —tensile strength of smooth joint; $Sj-coh$ —cohesion of smooth-joint; $Sj-\mu$ —friction coefficient of smooth joint

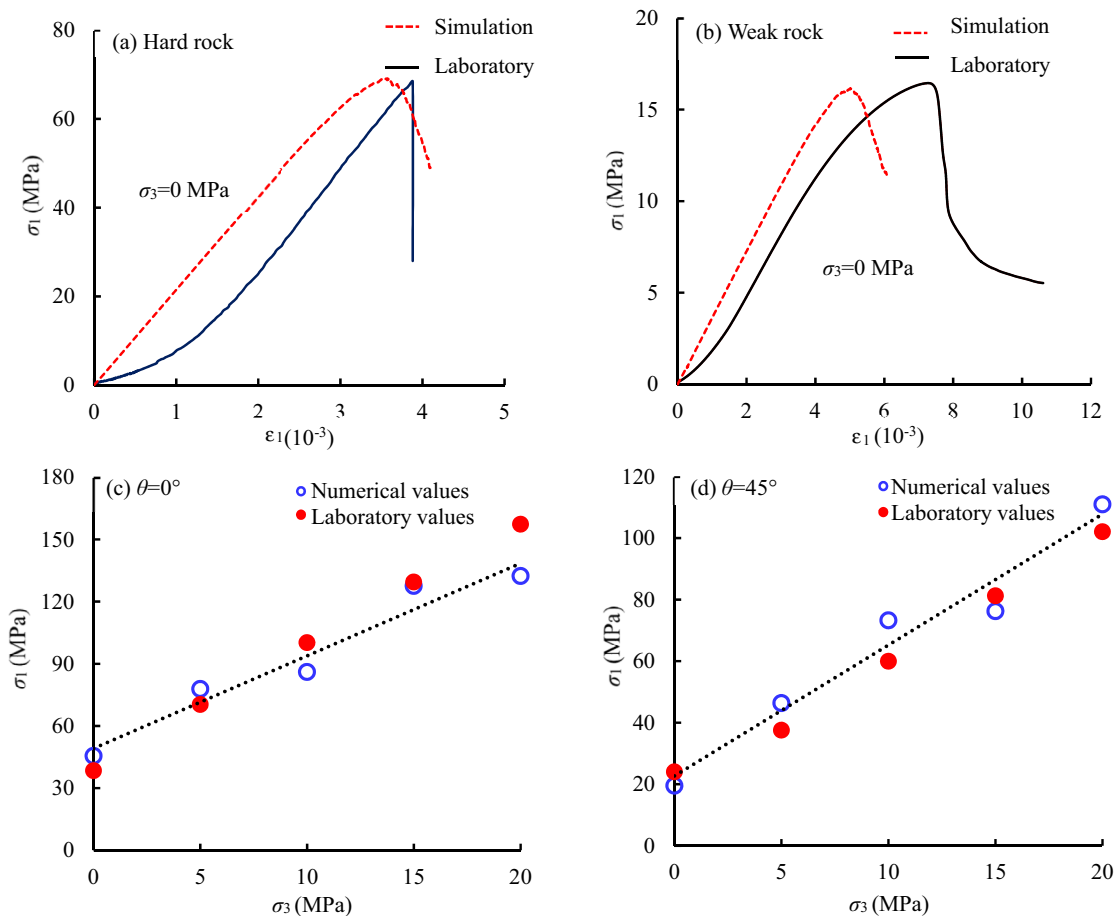


Fig. 5 Comparison of stress–strain curves between simulation and Laboratory test (Yang et al. 2019b) of (a) Hard rock and (b) Weak rock under uniaxial compression. Comparison of maximum principal

stress between numerical simulation and laboratory test of composite rock under triaxial compression with inclination of c θ_0° and d θ_{45°

the first stage are fixed, the cohesion and tension strength parameters are updated by trial-and-error method until the macroscopic peak strength of θ_0° specimens and θ_{45° specimens is in good agreement with the experiments. Figure 4 presents the flowchart of the calibration of composite rock, and the microscopic parameters are shown in Table 2.

The following is a comparative analysis of the simulation results and the corresponding laboratory tests. Figure 5 shows the comparison of stress–axial strain curves of complete hard and soft rock under uniaxial compression obtained from the experiment and 3D numerical simulation, respectively. Figure 5a and b shows that the curves obtained by simulation are basically consistent with the test results except for the initial compaction stage. Additionally, it can be clearly seen in Fig. 5c and d that the simulation results of the composite rock model are very close to the test values, except that there is a slight difference when the confining pressure of the composite rock with the bedding angle of θ_0° is 20 MPa. In a word, the calibration results show that the above micro-parameters can well reflect the properties of real test samples.

3 Mechanical Behavior Analysis of Composite Rock-Like Specimens

3.1 Strength and Deformation Properties

The deviatoric stress–axial strain and deviatoric stress–circumferential strain curves for all of the composite rock-like model from the bedding inclination of θ_0° to θ_{90° are shown in Fig. 6a–g. Overall, the deviate stress of rock-like models with different bedding inclination angles increased regularly with the increase of confining pressure, and the axial strain and circumferential strain enlarged significantly with the increase of circumferential pressure; almost all the graphs showed such a rule that brittle failure under low confining pressure gradually developed to ductile failure under high confining pressure. From a local perspective, the composite rock model with an inclination of θ_{60° and an inclination of θ_{75° showed obvious ductile mechanical behavior compared with other rock models, especially when the confining pressure was 20 MPa. This is because the confining pressure tightly presses the bedding plane between the soft and hard rock layers, causing significant retardation of the shear damage that should have occurred. It is worth noting that the uniaxial compression simulation curve of the composite rock model with an inclination of θ_{75° showed ductility; however with the increase of confining pressure, it did not show the expected obvious ductility but a brittle mechanical behavior. It is very interesting that almost all the curves had no stress drop before

the peak strength, and the composite rock-like models with θ_{75° and θ_{90° inclination angles existed violent stress fluctuations after the peak strength when the confining pressure was 15 MPa and 20 MPa. Besides, the deviatoric stress–circumferential strain curves showed a similar law.

It can be seen from Fig. 7 that the simulated maximum principal stress strength of different bedding angles under different confining pressures was generally consistent with the experimental results. However, the experimental value was significantly higher than the simulated value when the inclination was θ_{90° , and this phenomenon slightly decreased with the increasing of confining pressure. On the contrary, when the inclination was θ_0° and θ_{15° , the simulated peak strength was consistent with the experimental results when the confining pressure was small, However, with the increase of confining pressure, the numerical value obtained by simulation was larger than the experimental value, and the difference gradually increased. Besides, the numerical simulation failure strength variation displayed a “U” type clearly with inclination angle under different confining; this is in agreement with the conclusions drawn from the previous studies on the mechanical properties of transversely isotropic rock mass (Cho et al. 2012; Cheng et al. 2017, 2018; Yin and Yang 2018; Sapari and Zabidi 2019; Yang et al. 2019b). Both numerical simulations and experiments obtained the lowest values of failure strength at the inclination angle of θ_{60° and the highest values at angles of θ_0° and θ_{90° ; however, contrary to the indoor experimental results, the failure strength derived from numerical simulations was greater at θ_0° than at θ_{90° .

Figure 8 shows the peak axial strain of the composite formation model with different dip angles under different surrounding pressures. The peak axial strain presented a similar pattern with increasing dip angle at different enclosing pressures, with the maximum peak axial strain at θ_{15° and the minimum at θ_{60° in a wavy shape. Meanwhile, the peak strain increased uniformly with the increasing of the enclosing pressure, except for the θ_{60° composite rock with 0 MPa and 5 MPa enclosing pressure.

3.2 Ultimate Failure Modes Comparison

Figure 9 lists a part of ultimate failure modes comparison between simulation and laboratory results; the red balls represent macro-crack, which is controlled by the Coulomb criterion. When any of the normal, shear, torsional or bending moments exceed their limits, the bond will break and the color of the particles will be discriminated as red. Additionally, the white and black balls embody fine hard and weak rock matrix of numerical models, respectively. It can be observed that when both the soft and hard rock

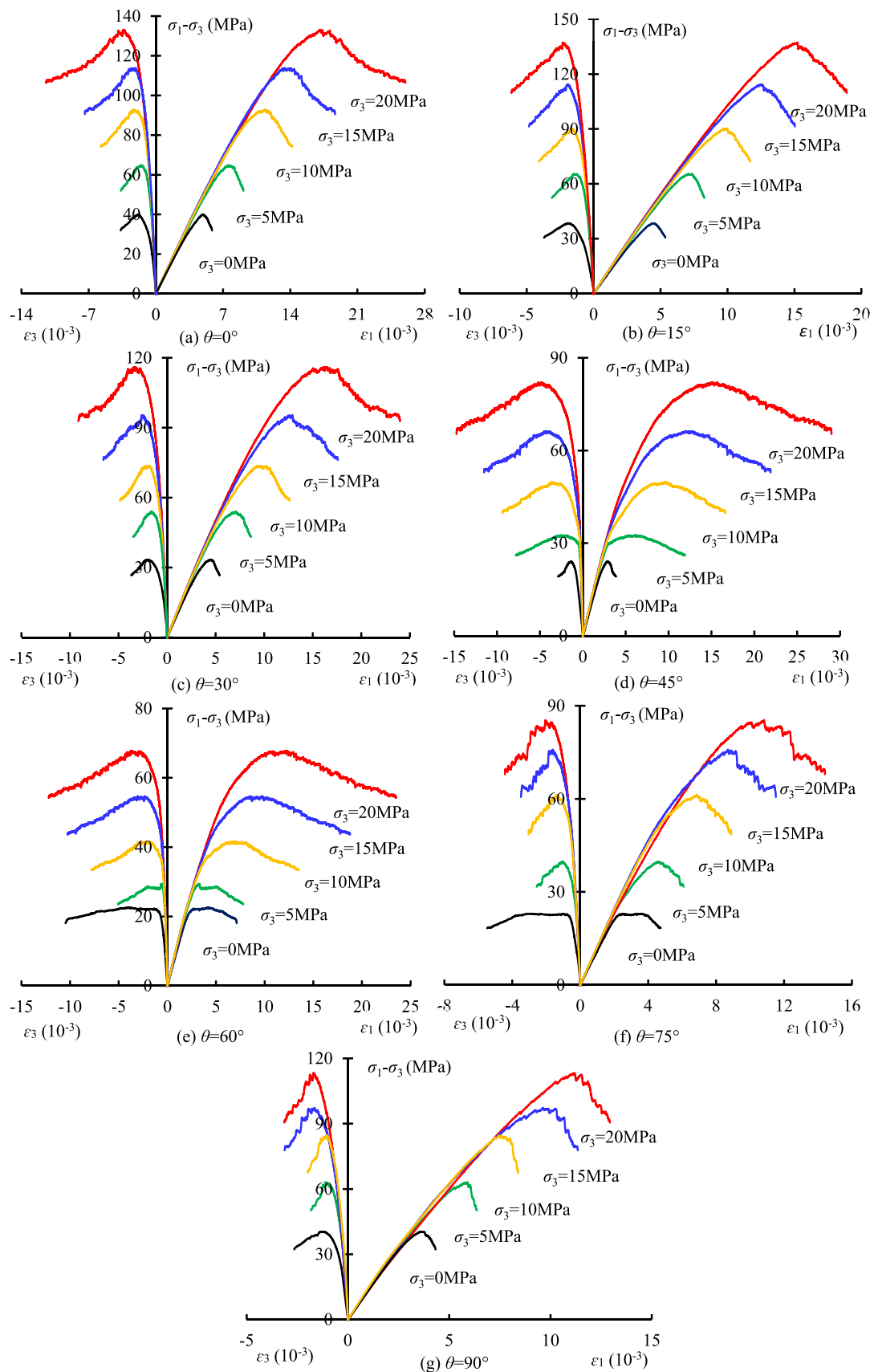


Fig. 6 The deviatoric stress–strain curves for composite models under different confining pressures with bedding angle of θ_0° , θ_{15° , θ_{30° , θ_{45° , θ_{60° , θ_{75° and θ_{90°

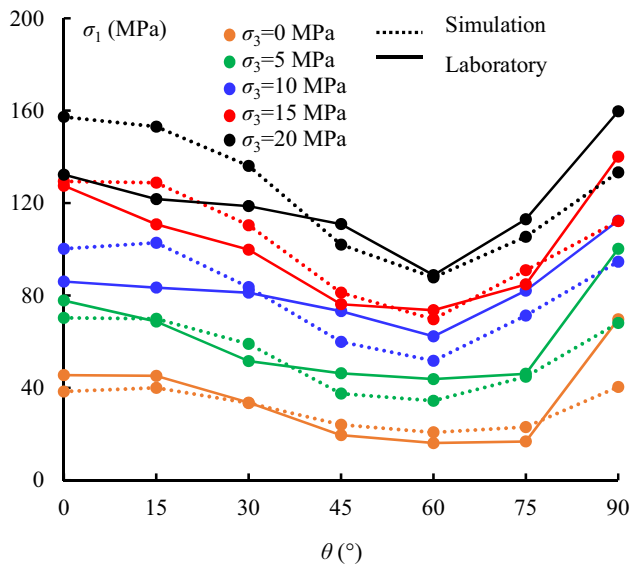


Fig. 7 Comparison of peak strength of maximum principal stress of composite rock under different confining pressures between numerical simulation and indoor test with increasing inclination angle

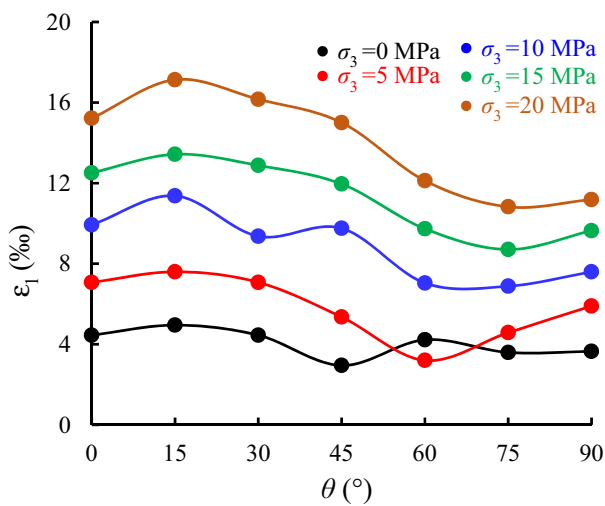


Fig. 8 The peak axial strain exhibited by the composite rock model with increasing bedding angle under different confining pressures by numerical simulation

layers were horizontal, the macroscopic damage diagrams obtained from the experiments showed that the specimens were splitting in tension through the layers under uniaxial compression, and as the surrounding pressure increased to 5 MPa and 20 MPa, the damage mode of the specimens gradually changed to shear damage pattern, and the angle between the shear section and the horizontal gradually decreased. When the dipping angle of the bedding was

θ_{90° for both the specimen and the model, the damage patterns were basically the same as that of the specimen with a laminar inclination of θ_{0° , except that the final damage pattern obtained from the numerical simulations and the indoor tests was splitting along the bedding surface when the confining pressure is 0 MPa; furthermore, we can see that the damage patterns obtained from the numerical simulations and the laboratory were identical when the inclination is θ_{60° . Additionally, what is remarkable is that all the macroscopic cracks obtained from the numerical simulations were much wider, which mainly resulted from the large discrete particle radius with generously sized.

4 Internal Fracture Behavior of Composite Rock-Like Specimens

4.1 Internal Spatial Crack Images Obtained by X-ray CT Reconstructing and Particle Modeling

To provide an in-depth analysis of the damage pattern and the crack extension mechanism of the composite material-like rock specimens, the internal cracking of the model is investigated in detail in this chapter and compared with the X-ray CT images of the test results, where the X-ray CT images were done by Yang et al. (2019b).

Figure 10 presents a series of internal spatial crack maps obtained from X-ray CT (gray) reconstruction and PFC^{3D} simulations (blue) from θ_{0° to θ_{90° of inclination at different confining pressures. When the specimens were under uniaxial compression, it is clear that the internal cracking patterns were almost identical in both the simulation and X-ray CT results: the internal crack at the bedding angle of θ_{0° , θ_{15° and θ_{30° exhibits that tensile damage and splitting failure crossed the hard rock and weak rock clearly; the following composite specimens with angle from θ_{45° to θ_{75° contained a lot of shear crack and the shear damage occurred mainly along the weak bedding surfaces. Besides, the shear crack mainly existed in weak rock area which can be observed in the modeling results at the inclination of θ_{45° and θ_{60° in particular. When the lamellar surface was perpendicular to the end face of the specimen, several splitting fractures were shown in the results of both the X-ray CT images and PFC^{3D} images. Therefore, it can be inferred that almost all the composite models are first damaged in soft rock area, followed by cracking in the hard rock area, and ultimate failure occurs.

When the confining pressure increased to 5 MPa, we can observe that the cracks in the soft rock in the θ_{0° to θ_{30° specimens became significantly sparser and more dispersed, but the damage pattern was essentially the same as in uniaxial compression, except that there were more and smaller

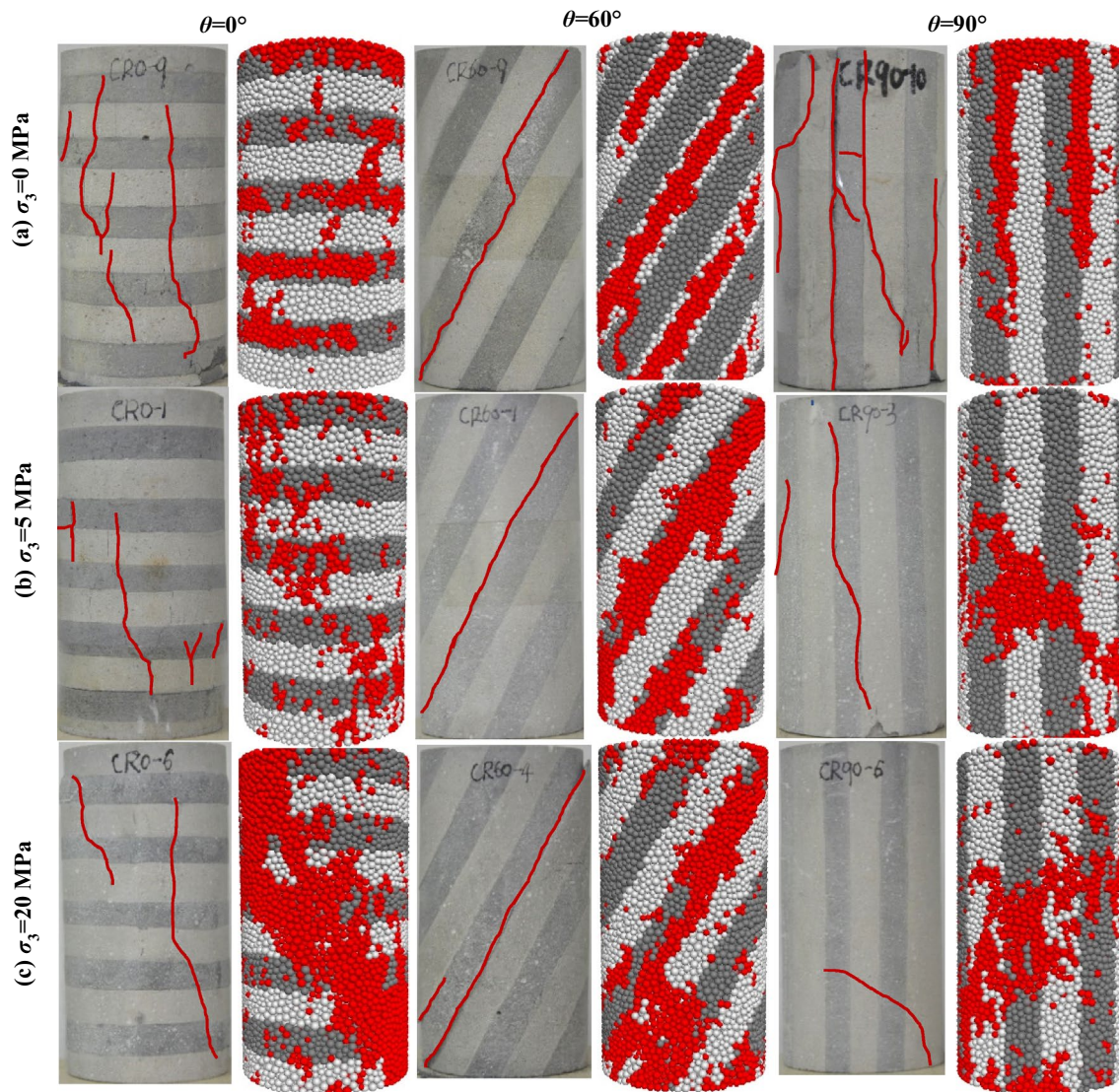


Fig. 9 Comparison of macro-failure mode of composite specimen obtained from laboratory experiment and PFC^{3D} simulation. The experimental results were obtained from Yang et al.

tensile cracks and splitting cracks in the specimen at angel of θ_{0° ; the same situation occurred in the θ_{45° to θ_{75° specimens, where the shear cracks were still concentrated in the central soft rock area, but it is clear that some cracks were also present in the hard rock section; from the result of X-ray CT images, the splitting failure crack became smaller compared to the specimen with a bedding angle of θ_{90° under uniaxial compression test.

Figure 10 shows the variation of inner crack of simulation and X-ray CT images with a higher confining pressure (20 MPa). It can be seen that the cracks were already almost all over the model at high envelope pressures; whereas, the number of cracks was significantly reduced in the 3D image constructed from the X-ray CT, which is actually due to the

high threshold set for the CT scan, resulting in very small cracks not being detected. In addition to these, at lower laminar inclination angles of the specimens, there were almost no tensile cracks accumulation between the soft and hard rocks; similarly when the angle increases to θ_{45° to θ_{75° , shear cracks were still present but were clearly inhibited by the surrounding pressure and the number of cracks in the hard rocks increased significantly. However, when the inclination angle reached θ_{90° , the crack distribution of the model differed significantly from the CT diagram, that is, the X-ray CT three-dimensional reconstruction showed a trace of cracking in the middle of the model, but the pattern of failure mode was invisible. However, the PFC^{3D} model showed a shear damage pattern clearly. It is worth noting

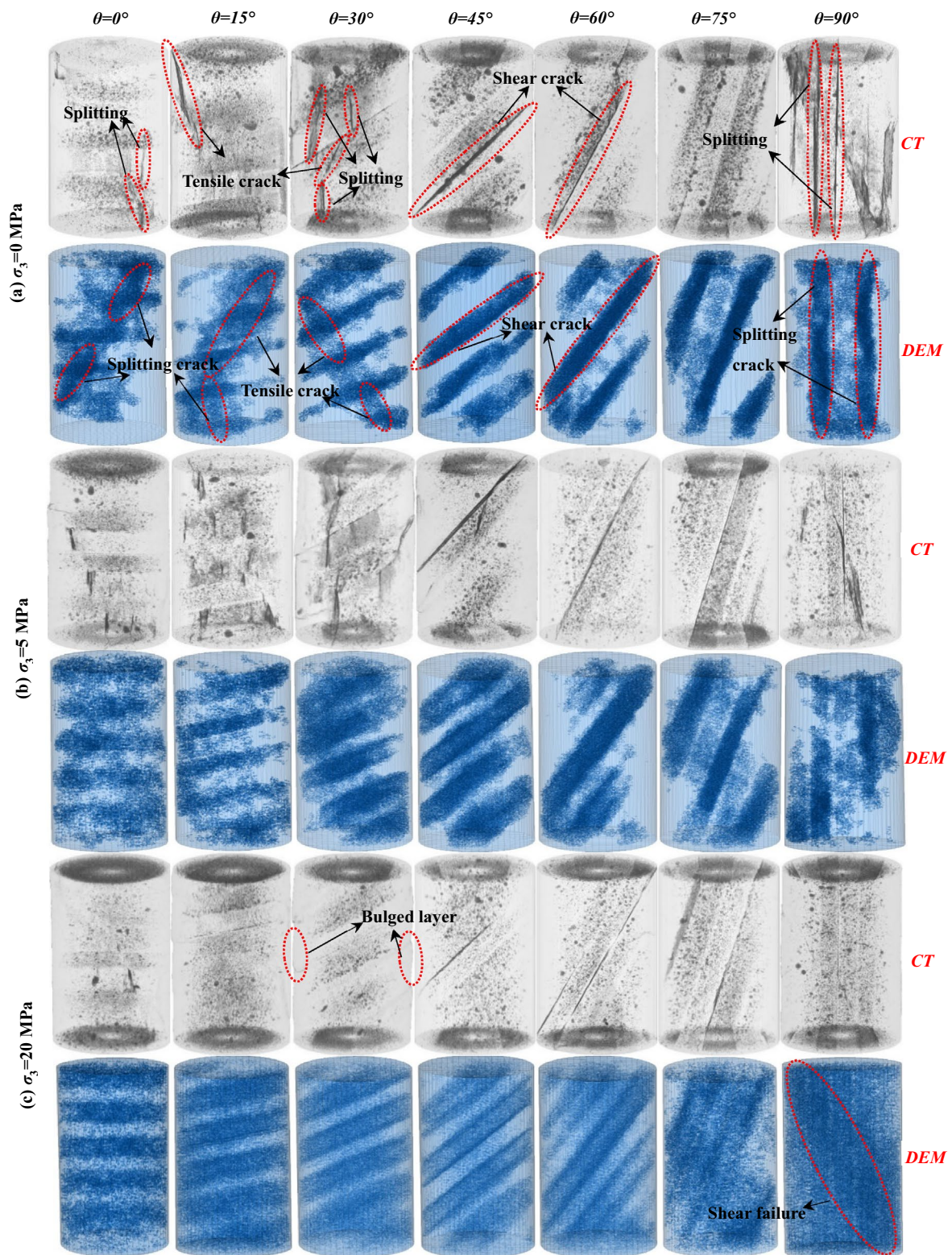


Fig. 10 Comparison of internal crack obtained by X-ray CT (Yang et al. 2019b) and modeling from bedding angle of θ_0 to θ_{90} under different confining pressures

that the sidewalls at the cylindrical soft rock of the damaged specimens obtained from the actual tests bulged significantly, but the numerical simulations did not have this effect, which is due to the rigid walls used in PFC^{3D}.

4.2 Vertical and Horizontal Cross Sections Obtained by X-ray CT Scanning and Simulation

The information acquired by the spatial crack pattern is negligence and restricted, it might be premature to declare that we have mastered all the characteristics of internal cracking.

Therefore, the analysis of crack patterns in cross section images is necessary. Three representative sets of vertical and horizontal cross-section images are selected to investigate the failure mechanism more comprehensively (presented in Figs. 11 and 12), where the vertical section is obtained at $Z=50$ mm (on the top of hard rock matrix) and the horizontal section is obtained at $X=25$ mm. The schematic diagram of spatial section is shown in Fig. 12a.

The information gathered from the cross section (Fig. 11a and b) strengthen our confidence in the descriptions drawn from the three-dimensional spatial crack chart.

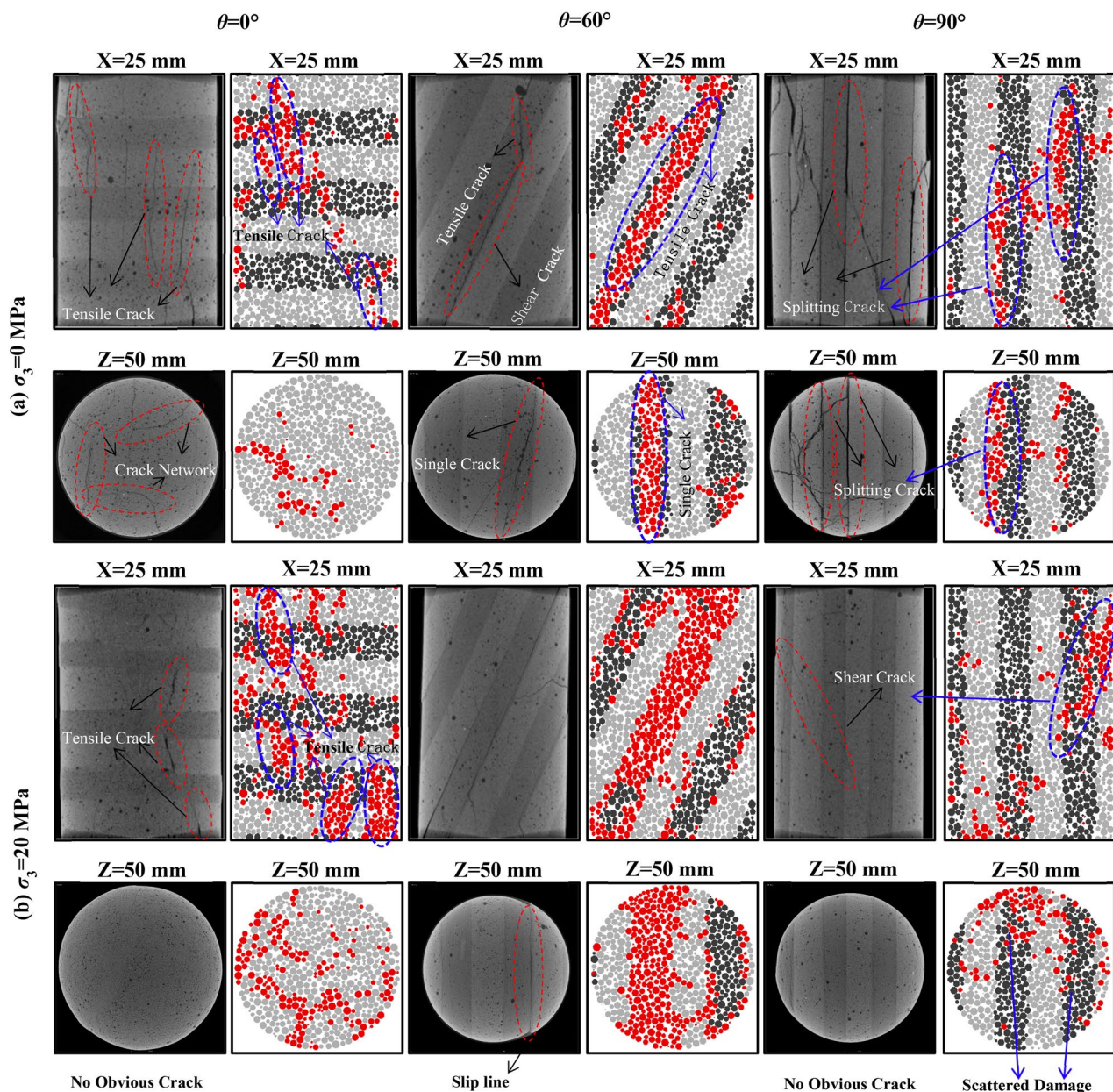


Fig. 11 Comparison of crack behavior in cross section of three representative composite rock specimens (with bedding angle of θ_0° , θ_{60° , and θ_{90°) **a** under uniaxial compression test and **b** with confining pressure of 20 MPa between modeling and X-ray CT scanning

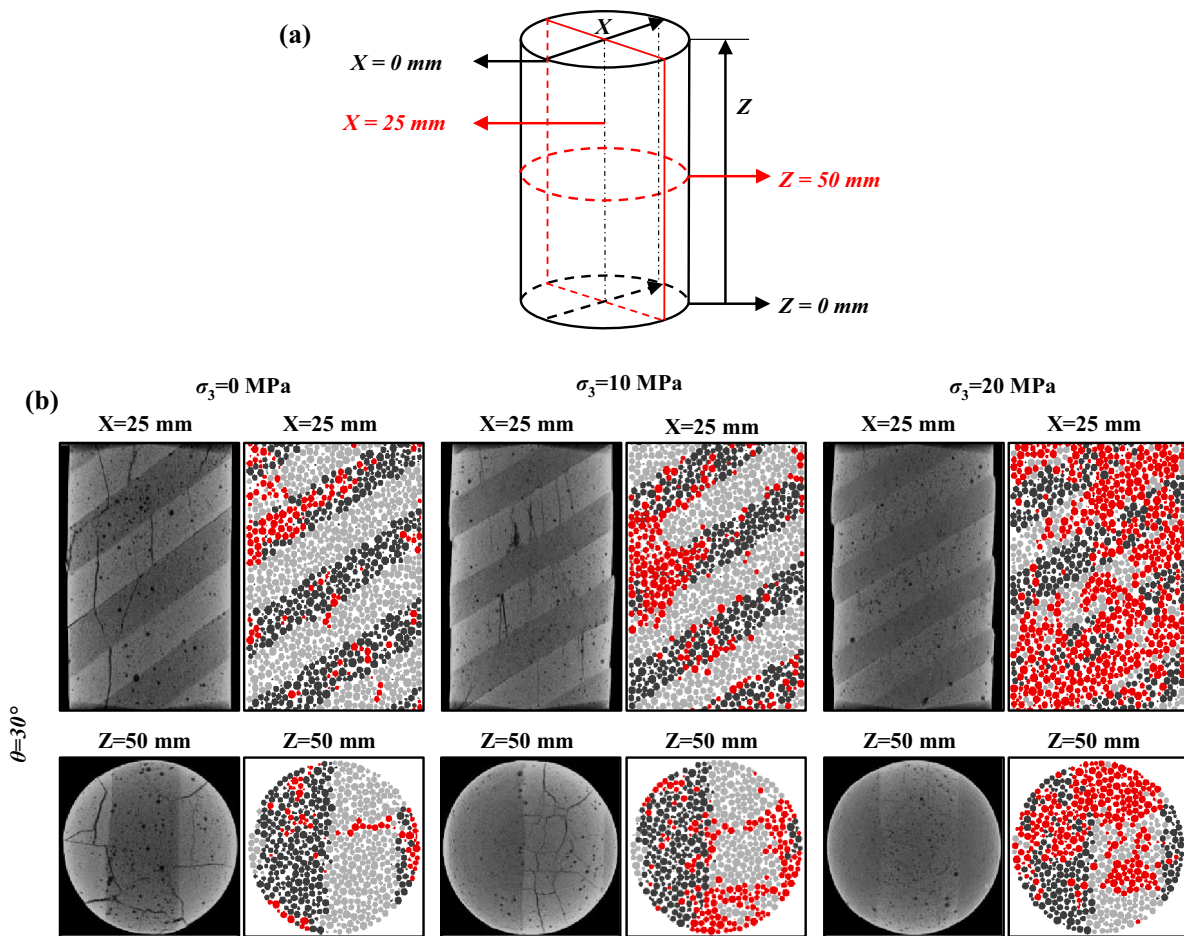


Fig. 12 Comparison of crack behavior in cross section of composite specimen with θ_{30° laminar angle under different confining pressures (0, 10, 20 MPa) between modeling and X-ray CT scanning

However, we manage to capture a few additional details from the horizontal cross sections. A fully developed fracture network on hard rock faces can be observed in the specimen with θ_{0° bedding inclination under uniaxial compression test, which indicates that the hard rock was sufficiently deformed to permit brittle failure. In contrast, at a laminar dip of θ_{60° we can see a distinct single crack in the soft rock bar, which was consistent with the CT image. Besides, the splitting crack occurred at the junction of soft and hard rocks in the composite rock model with a θ_{90° laminar angle, while more tensile cracks extended in hard rock bars as the hard rock was subjected to the main axial stresses. However, with the confining pressure increasing of 20 MPa (shown in Fig. 11b), there were no obvious crack in X-ray CT charts but more decentralized failure balls in modeling images. To further figure out the causes of this phenomenon, a series of cross-sectional images (presented in Fig. 12) of specimen with θ_{30° angle

of weak plane under three different confining pressures (0, 10, 20 MPa) were studied. As the confining pressure growing, in vertical cross sections, the fracture behavior changed from large damage mainly in the soft rocks to minor damage both in the soft rocks and in the hard rocks, which was consistent with the X-ray CT images, though the cracks obtained from the test are too tiny to be seen with the naked eyes. However, in horizontal cross sections acquired from X-ray CT scanning, the crack disappeared as the confining pressure increased to 10 MPa, while a more widely distributed network was in the hard rock pillar. Additionally, it is worth mentioning that the horizontal cross sections of the specimens obtained by X-ray CT scanning at $Z=50$ mm significantly differed from those obtained by simulation in terms of the distribution of the different lithological compositions. This may be resulted by the large bulged layers in composite rock-like specimens. All in all, we can find that the confining pressure

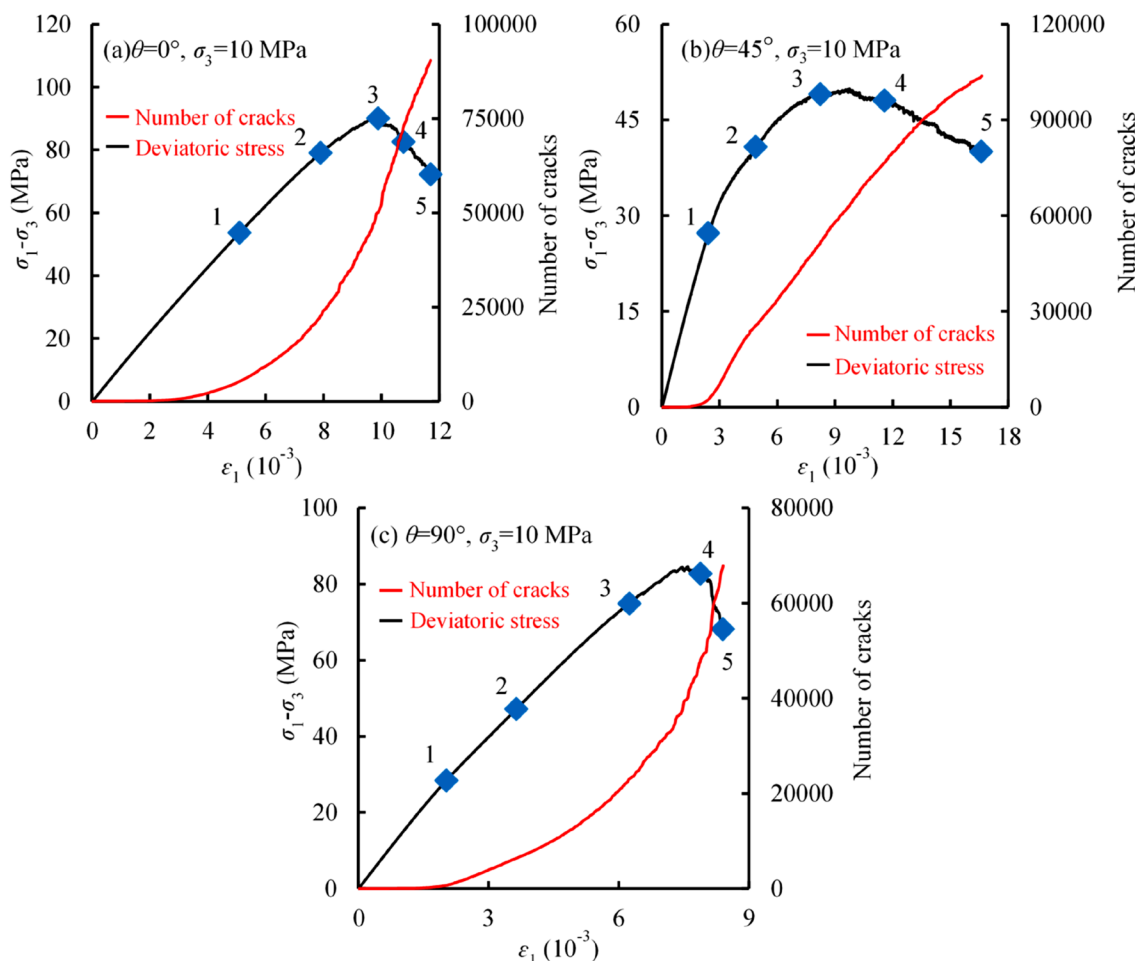


Fig. 13 Variation in the number of cracks in composite rock models at different dip angles under triaxial compression

reduced the difference in mechanical properties between soft and hard rock matrix.

The above two sections described the varies damage modes of composite rocks at different dip angles. Given the Mohr–Coulomb criterion used for both the rock and the parallel weak surfaces in this simulation, it seems reasonable to use the Jaeger’s criterion to explain above phenomenon.

$$\sigma_1 = \sigma_3 + \frac{2(c_w + \sigma_3 f_w)}{(1 - f_w \cot \beta) \sin 2\beta}, \tag{1}$$

where σ_1 and σ_3 are the principal compressive stress and confining compressive stress on specimens, c_w represents the cohesion of structural surfaces, $f_w = \tan \theta_w$, in which θ_w represents the internal friction angle of structural surfaces, and β means the bedding angle of weak plane. When the failure occurs in rock matrix, the formula can be rewritten as:

$$\sigma_1 = \sigma_3 + \frac{2(c_r + \sigma_3 f_r)}{(1 - f_r \cot \beta) \sin 2\beta}, \tag{2}$$

where c_r represents the cohesion of rock matrix, $f_r = \tan \theta_r$, in which θ_r represents the internal friction angle of rock matrix.

Through the geometric relationship in Mohr stress circle, we can derive:

$$\beta_1 = \frac{\theta_w}{2} + \frac{1}{2} \arcsin \left[\frac{(\sigma_1 + \sigma_3 + 2c_w \cot \theta_w) \sin \theta_w}{\sigma_1 - \sigma_3} \right]. \tag{3}$$

Similarly, it can be obtained that:

$$\beta_2 = \frac{\pi}{2} + \frac{\theta_w}{2} - \frac{1}{2} \arcsin \left[\frac{(\sigma_1 + \sigma_3 + 2c_w \cot \theta_w) \sin \theta_w}{\sigma_1 - \sigma_3} \right]. \tag{4}$$

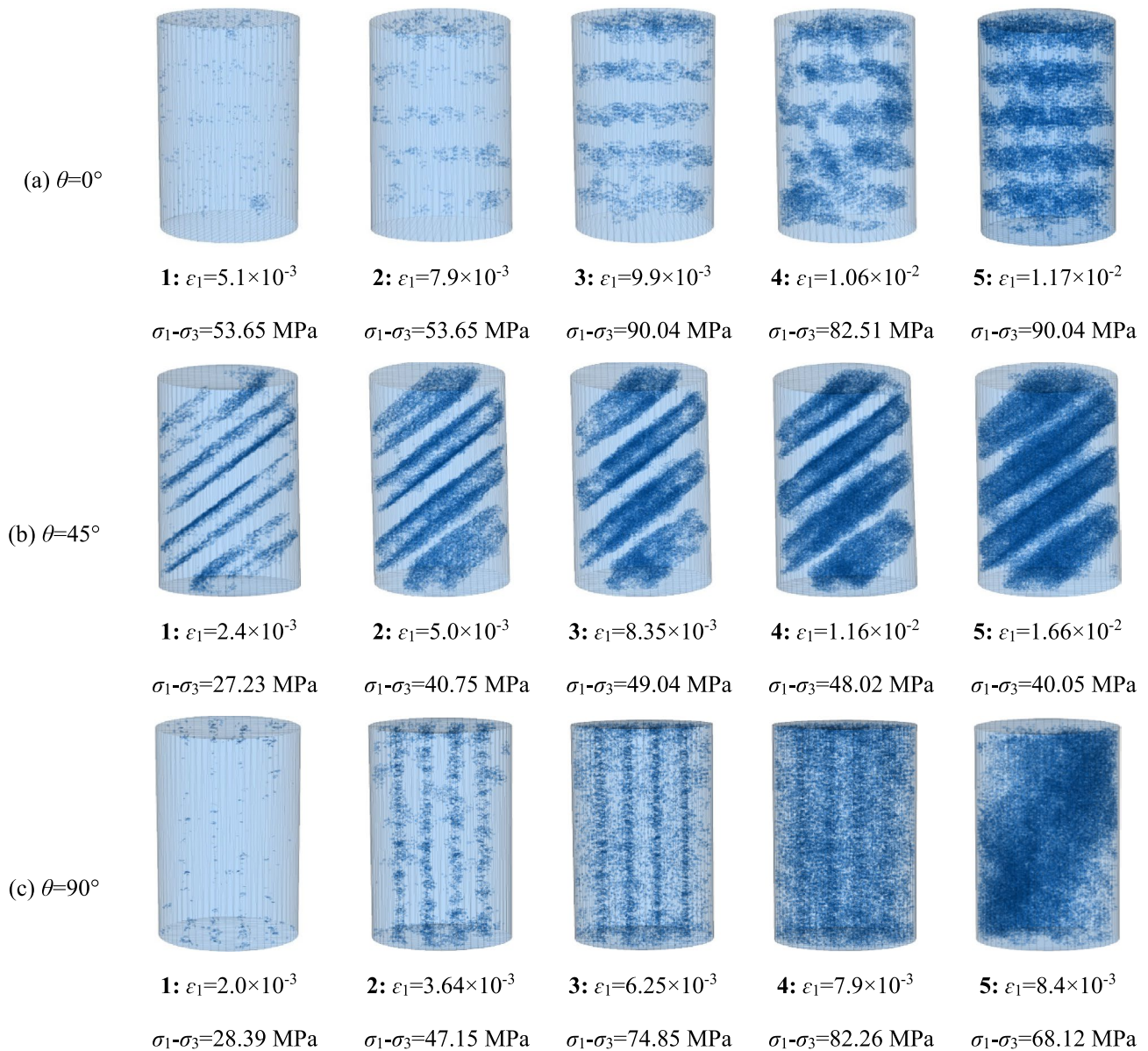


Fig. 14 Crack coalescence process of composite rock models with different bedding angles under confining pressure of 10 MPa

Jaeger stated that when $\beta < \beta_1$ or $\beta > \beta_2$, the rock will not break along the structural face, where the strength of the rock depends on the strength of the bedrock part, independent of the presence of the structural face; when $\beta_1 < \beta < \beta_2$, the rock will break along the weak side and the compressive strength is reduced relative to other angles (Jaeger 1960). Our simulations fit this theory perfectly.

4.3 Crack Coalescence Process with Different Bedding Angles

The study of crack evolution in composite rock formations is a highlighted advantageous of numerical simulation, as it

reflects crack emergence under certain stress as well as certain strain condition, which in turn assist us to gain insight into the extent of damage to composite rock formations in practical engineering. The growth profile of the number of cracks corresponding to the stress–strain curves of the composite models with three different angles under confining pressure of 10 MPa is plotted in Fig. 13 where the black curves represent the stress corresponding to strain and the red curves represent the number of cracks. Five points are set on the stress–strain curves to reveal the crack coalescence process.

Two types of growth curves of the number of cracks are shown in Fig. 13: one is hypo concave curve corresponding to

the models with a laminar inclination of θ_{0° and θ_{90° ; another is nearly linear type plotted in Fig. 13b. During the initial elastic loading phase, the number of cracks in the lower concave curve was significantly less than in the linear curve, due to the large number of shear cracks sprouting as a result of slip damage along the laminae at the beginning of elastic loading phase of the model with an inclination angle of θ_{45° . However, as the elastic phase progressed, the growth rate of the number of cracks increased substantially for the models with θ_{0° and θ_{90° laminar dip angles until the rock models were destroyed. Moreover, the number of cracks in Figs. 10b and c, 13a was roughly 50000, 65000, and 48000, respectively, when the peak strength point was reached; however, the final number of cracks was approximately 90000, 100000, and 67000, respectively, due to the high ductility of the θ_{45° composite rock model.

The internal crack evolution of the three specimens with different bedding dips under the confining pressure of 10 MPa is shown in Fig. 14, where it can be seen that the cracks in the

specimens with a laminar dip of θ_{0° appeared first in the soft rock layers and evolved slowly in number, and cracks starting to appear in the hard rock when the axial strain reached 1.06×10^{-2} . However, the shear fractures appeared first along the bedding planes in Fig. 14b, then emerged in the soft rock area substantially, and showed in the hard rock after the peak stress strength ultimately. Additionally, the cracking process of composite model with an inclination of θ_{90° under 10 MPa is presented in Fig. 14c. In the diagrams corresponding to the first two points, only very few cracks appeared at the vertical laminated surfaces, and in the two images set up afterwards, the cracks grew in both the soft rock and the hard rock. Besides, it can be seen that the fracture number conceived dramatically from point 4 to point 5. In addition to this, the composite rock models with dips of θ_{0° as well as θ_{90° had significantly less cracks at the first three points than the model with a θ_{60° laminar dip, which was consistent with the previous analysis.

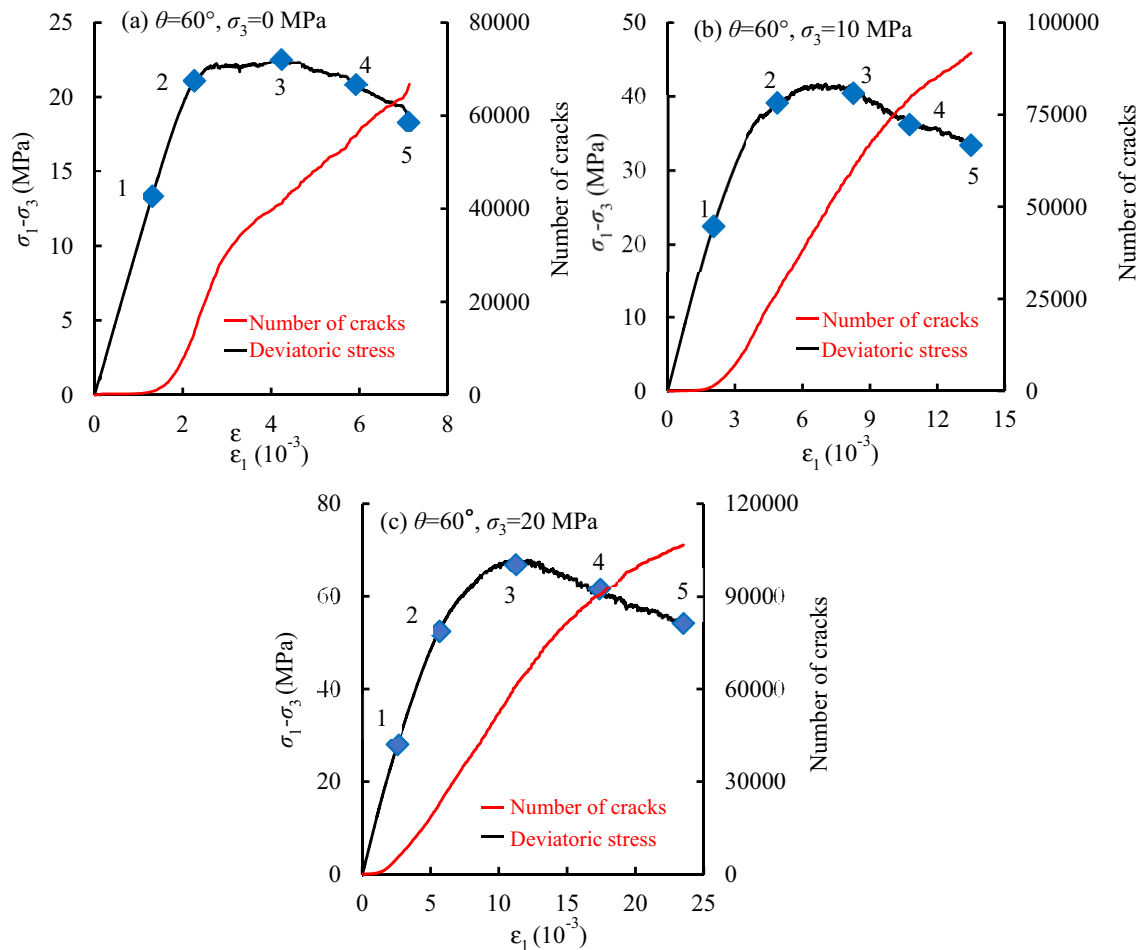


Fig. 15 Variation in the number of cracks in composite rock models under different confining pressures at the inclination of θ_{60°

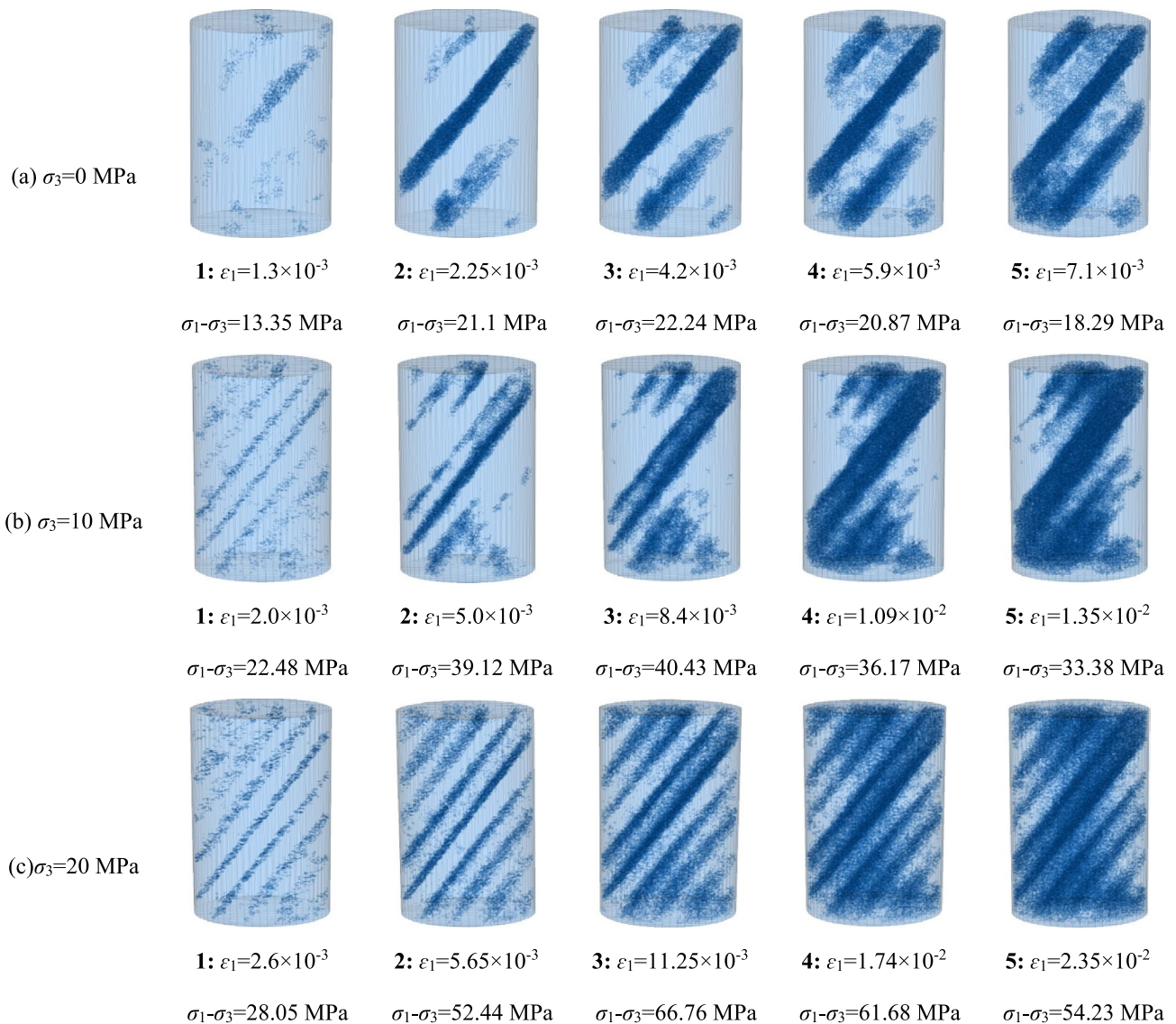


Fig. 16 Crack coalescence process of composite rock models with bedding angles of θ_{60° under different confining pressures

4.4 Crack Coalescence Process Under Different Confining Pressures

In this section, the influence of different confining pressures on the cracking process of composite rock model is investigated. Figure 15 images three diagrams of crack number corresponding to stress–strain of composite rock models under different confining pressures (0, 10, 20 MPa) with bedding angle of θ_{60° , and the inner micro-crack coalescence of these models is presented in Fig. 16 which is divided into five points.

Figures 15a and 16a show the crack coalescence process of the specimen with bedding angle of θ_{60° under uniaxial

compression simulation. In the first point ($\epsilon_1 = 1.3 \times 10^{-3}$, $\sigma_1 - \sigma_3 = 13.35$ MPa), it can be seen that there were only few cracks from the three-dimensional micro-crack image and the number of micro-fractures was 2584. However, the process from the first to the second point ($\epsilon_1 = 2.25 \times 10^{-3}$, $\sigma_1 - \sigma_3 = 21.1$ MPa) produced a large number of cracks, growing to 19601 in number and concentrated mainly as one shear crack in the central soft rock area. Subsequently, the number of cracks increased at an almost constant rate until it hits the peak number of 66,755 at the fifth point ($\epsilon_1 = 7.1 \times 10^{-3}$, $\sigma_1 - \sigma_3 = 18.29$ MPa).

The situation changed considerably when the surrounding pressure increases to 10 MPa; the cracks first appeared

in the central part of the model at the both upper and lower laminated faces of the soft rock when the axial stress was 2.0×10^{-3} and deviatoric stress was 22.48 MPa. Additionally, the inner micro-cracks were initiated around the weak rock area in the middle of the composite rock model, and the number of the cracks reached 31572 in the third point. When the axial strain exceeded 1.09×10^{-2} , the micro-cracks at the top and bottom ends of the numerical model propagated rapidly, resulting in three macroscopic shear cracks that emerged in the soft rock area. In the last point ($\epsilon_1 = 1.35 \times 10^{-2}$, $\sigma_1 - \sigma_3 = 33.38$ MPa), all the micro-cracks in the three-dimensional model coalesced to form a “Z”-shaped damage pattern, and the total number of cracks reached 91762.

Ultimately, as shown in Figs. 15c and 16c, the cracks of composite rock specimen with a higher confining pressure (20 MPa) were characterized by wider distribution, less dense, larger quantities and more challenge to distinguish the major crack pattern. In the first point ($\epsilon_1 = 2.6 \times 10^{-3}$, $\sigma_1 - \sigma_3 = 28.05$ MPa), almost all the bedding plane initiated micro-cracks and the exact number of them was 6208. Following is the point 2 with the deviatoric stress of 52.44 MPa, the fractures number increased to 21470. As the specimen was loaded to point 3 (peak stress strength point), it can be seen that all the weak rocks were damaged to a certain extent. Shortly afterwards, the stress–strain curve dropped to point 4 and point 5, the increasing number of cracks expanded in the hard rock, and the final number of micro-cracks was 106629 at the strain of 2.35×10^{-2} .

5 Comparison of Stress Variation Between Soft And Hard Rock Formations

The previous chapter showed that the internal cracking pattern of composite rock samples is dramatically subject to both different layering dips and changing confining pressures, and to further illuminate the reasons for this, this chapter will investigate the inner stress state of the hard and soft rock of the specimen. Two measure balls with radius of 4.0 mm were placed in the rock layers with different mechanical characteristics, and both of them were in the center of the models (Center coordinate of the specimens is (0, 0, 0), and the specimens with bedding angle of θ_{0° , θ_{45° , θ_{60° and θ_{90° were measured by balls with the coordinates of (0, 0, -0.005) and (0, 0, -0.005), (0, 0, 0) and (0, 0, 0.013), (0, 0, 0.005) and (0, 0, -0.01), (0, -0.005, 0) and (0, 0.005, 0), respectively.)

5.1 Internal Stress State of Composite Rock Models with Different Inclinations

Figure 17 presents the measurement results of normal stress in three principal directions (σ_x , σ_y , σ_z) in hard and soft rock layers of composite models with various bedding angle under confining pressure of 10 MPa. When the inclination of model is θ_{0° , it can be seen that the Z-directional normal stress was slightly higher in hard rocks than in soft rocks, although the measured outputs in both lithologies showed close normal stresses in the X and Y directions, the two normal stresses increased incrementally in hard rocks and decreased progressively in soft rocks. In contrast to the above, the Z-directional normal stress was lower in hard rocks than in soft rocks at a laminar dip of θ_{45° , and σ_x and σ_y exhibited a significant difference at the peak stress point, i.e., σ_y was greater than σ_x , especially in soft rocks. Furthermore, the σ_z of the hard rock was markedly greater than that of the soft rock when the dip of the laminae coincided with the direction of pressurization, while the normal stresses in the Y and X directions for both remained roughly constant at 10 MPa.

At the same time, the results of the tangential stress (τ_{zy} , τ_{yx} , τ_{xz}) measurements are diagrammed in Fig. 18 As can be seen, the measured shear stresses in the soft and hard rocks were noticeably different when the laminar dip angle of the model is θ_{0° , with the tangential stresses in the X–Y and X–Z planes in the hard rocks being continuously increasing negative tangential stresses, while the tangential stresses in the soft rocks were continuously increasing positive tangential stresses. Moreover, the τ_{zy} in hard rock initially remained around zero until the axial strain reached 8×10^{-3} and then suddenly increased to negative; whereas in soft rock, the τ_{zy} slowly increased to positive until the axial strain was 8×10^{-3} and then suddenly dropped rapidly to negative. In general, the τ_{zy} in hard rock was greater than in soft rock. Both hard and soft rocks showed the most pronounced variation in τ_{zy} when the model had a laminae dip of θ_{45° , but the τ_{zy} of hard rock was consistently greater than the soft rock, in comparison to hard rocks, the shear stress curves for soft rocks presented more stress drop phenomenon, and the tangential stresses in X–Y plane of both the hard rock and soft rock were in opposite directions. When the bedding angle of composite rock increased to θ_{90° , tangential stress of τ_{zy} and τ_{yx} barely acted in the hard rock region before the peak axial strain point, and only marginal τ_{zy} was detected in the soft rock areas. Meanwhile, the measured spheres in the hard rock displayed a jump in tangential stress of τ_{xz}

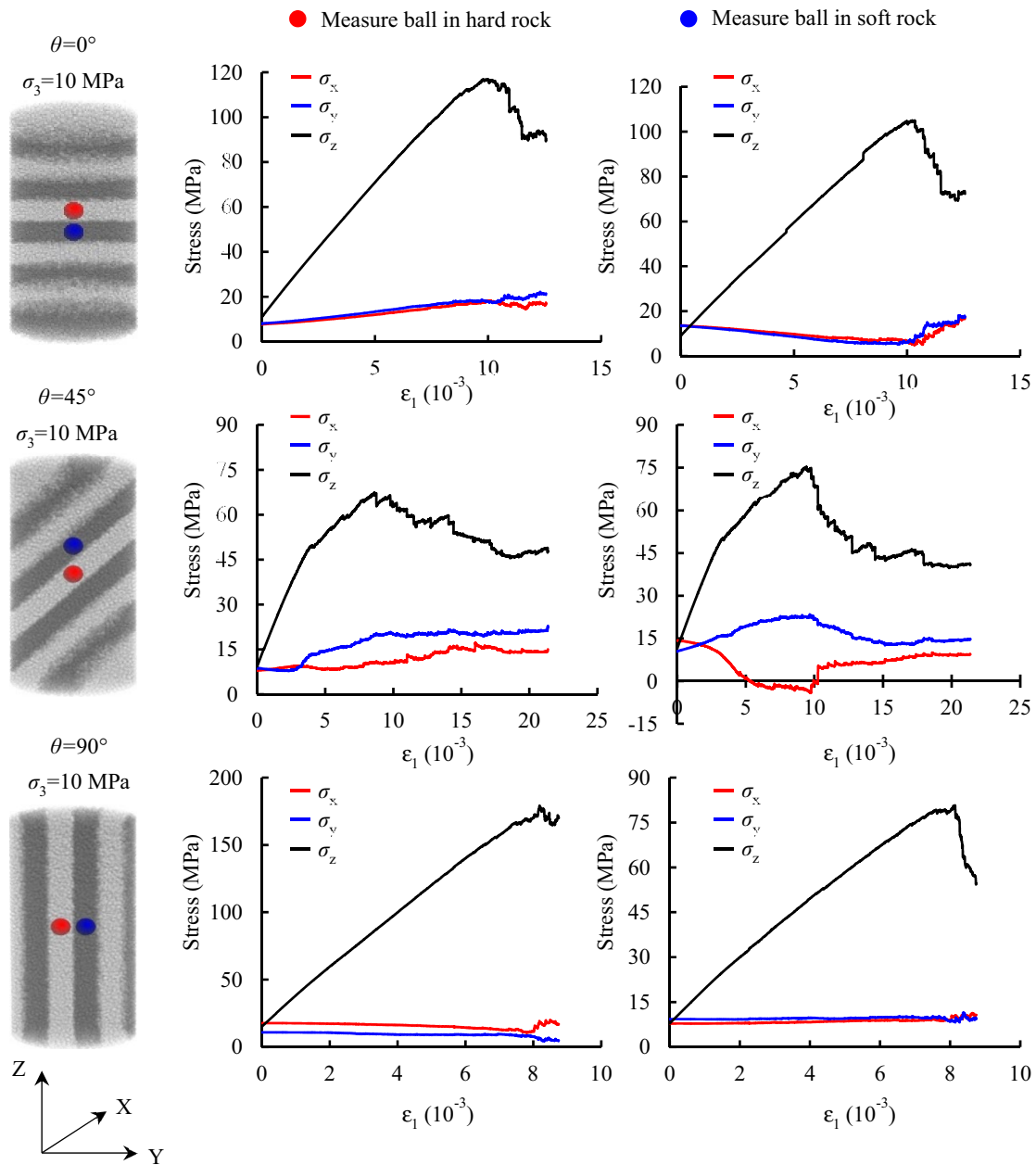


Fig. 17 Comparison of normal stress variation between soft and hard rock of the model with different bedding inclinations under confining pressure of 10 MPa

when the axial strain was 8×10^{-3} and the peak was visibly greater than the tangential stress in the soft rock; in contrast, τ_{zy} in soft rocks showed a sharp positive increase at the same point.

5.2 Internal Stress State of Composite Rock Models Under Different Confining Pressures

Figure 19 represents the measurement of normal stresses in both the hard rock and soft rock of the models with

inclination of θ_{60° under different confining pressures (0, 10, 20 MPa). The uniaxial compression results indicated that the axial principal stresses in the hard rock registered a number of drop-off points after reaching the peak strength, while those in the soft rock remained more or less level after reaching the top point. As axial compression was progressive, the normal principal stresses in the Y directions tended to increase and then fall in hard rocks; while in soft rocks, they were characterized by an increase and then a constant trend. Additionally, the σ_x in hard material expressed as tensile

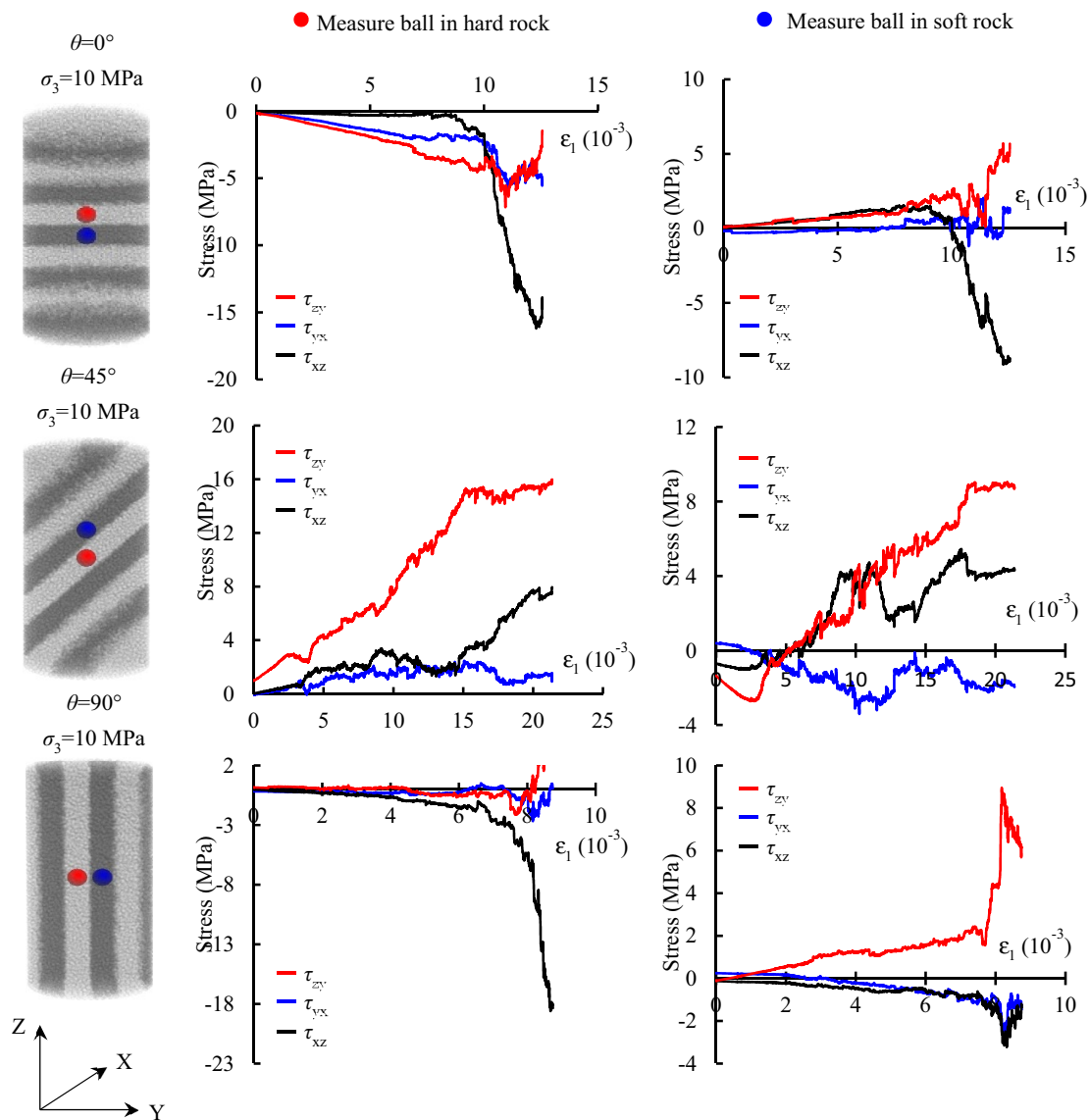


Fig. 18 Comparison of tangential stress variation between soft and hard rock of the model with different bedding inclinations under confining pressure of 10 MPa

stress which was contrast to σ_x in soft material. Besides, the normal stress curves measured in soft and hard rock at 10 MPa and 20 MPa were similar in pattern, in that the axial stress increased linearly and then decreased continuously; σ_y in the hard material increased before the peak strain point and then dropped, while the σ_y in the soft material increased to final point; σ_x characterized a symmetrical pattern with σ_y along the line of $\sigma = \sigma_3$ in the hard rock and remained a constant value of σ_3 in soft rock. It is worth indicating that the principal stresses in the X-direction transformed from

tensile stresses to compressive stresses as the confining pressure increased, and that the difference in axial stresses in the hard and soft rock formations became greater, i.e., the axial compressive stresses in the hard rock became greater than those in the soft rock due to the function of confining pressure.

The comparison of tangential stress measured in hard and soft rock of composite model with θ_{60° bedding angle under different confining pressures is plotted in Fig. 20. As was revealed in graph of composite model under uniaxial compression test,

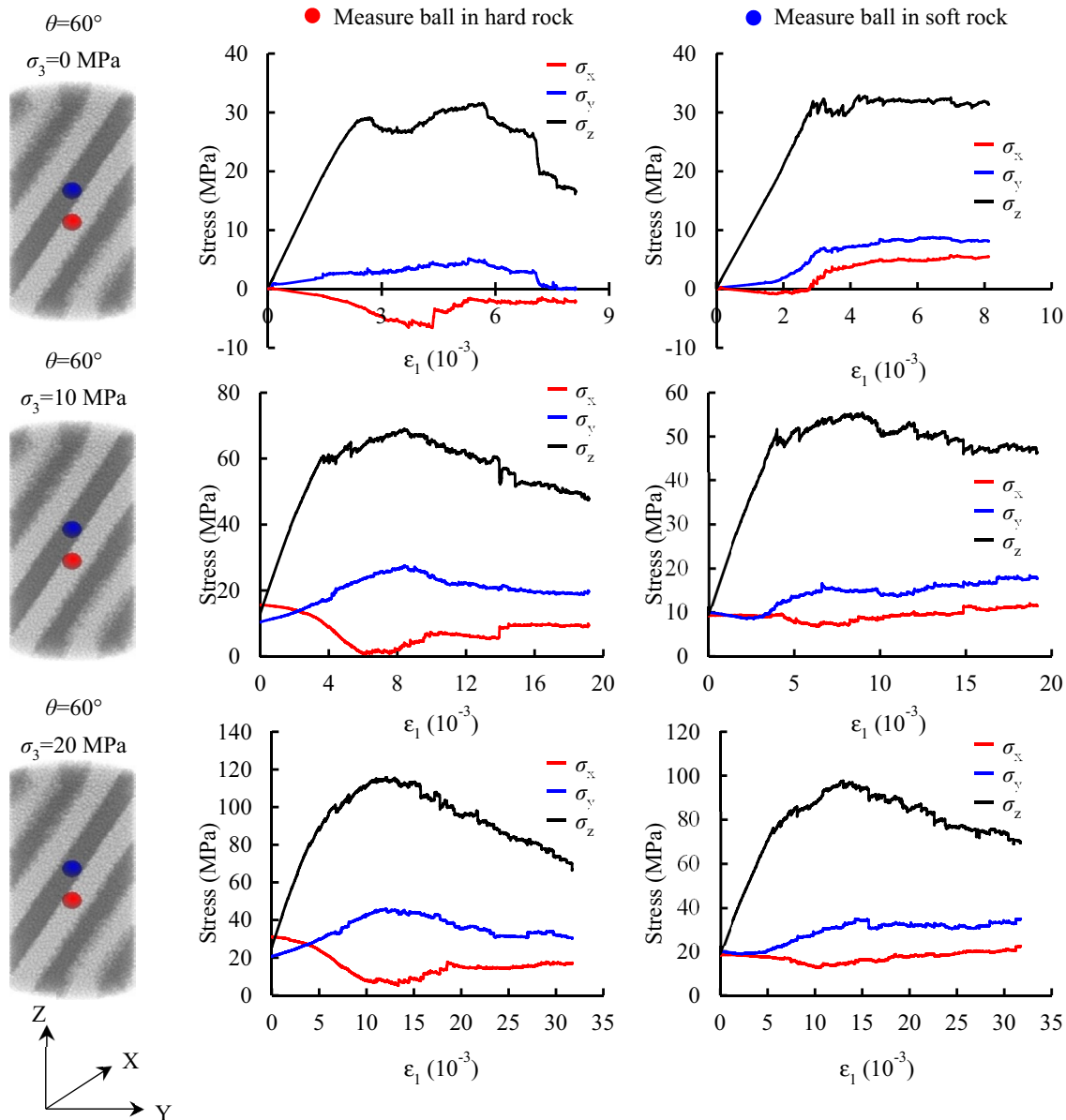


Fig. 19 Comparison of normal stress variation between soft and hard particles of the model with θ_{60° bedding inclination under different confining pressures

τ_{zy} fluctuated sharply all through the simulation compared to τ_{yx} and τ_{xz} , increasing rapidly before axial strain at 2×10^{-3} and dropping to zero in the vicinity of 7×10^{-3} of axial strain, but climbing again to the reverse direction in hard rock. In contrast to hard rock, τ_{zy} in soft rock underwent a continuous increase in the positive direction except for a stress drop between the axial strain of 2×10^{-3} and 3×10^{-3} . The key findings taken from the curves of triaxial compression tests under confining pressure of 10 MPa and 20 MPa were similar in patterns compared to the results of uniaxial compression simulation, but the curve of τ_{zy} hardly changed through the process.

6 Discussions

6.1 Implications for Safety of Interbedded Rock Slope

Stratified natural slopes are very common and are generally divided into reverse slopes, prograde slopes, and vertical slopes (shown in Fig. 21). The presence of laminated weak surfaces makes interlaminated slopes more susceptible to failure, and in fact, these slopes have already undergone a long and complex stressing process during their formation,

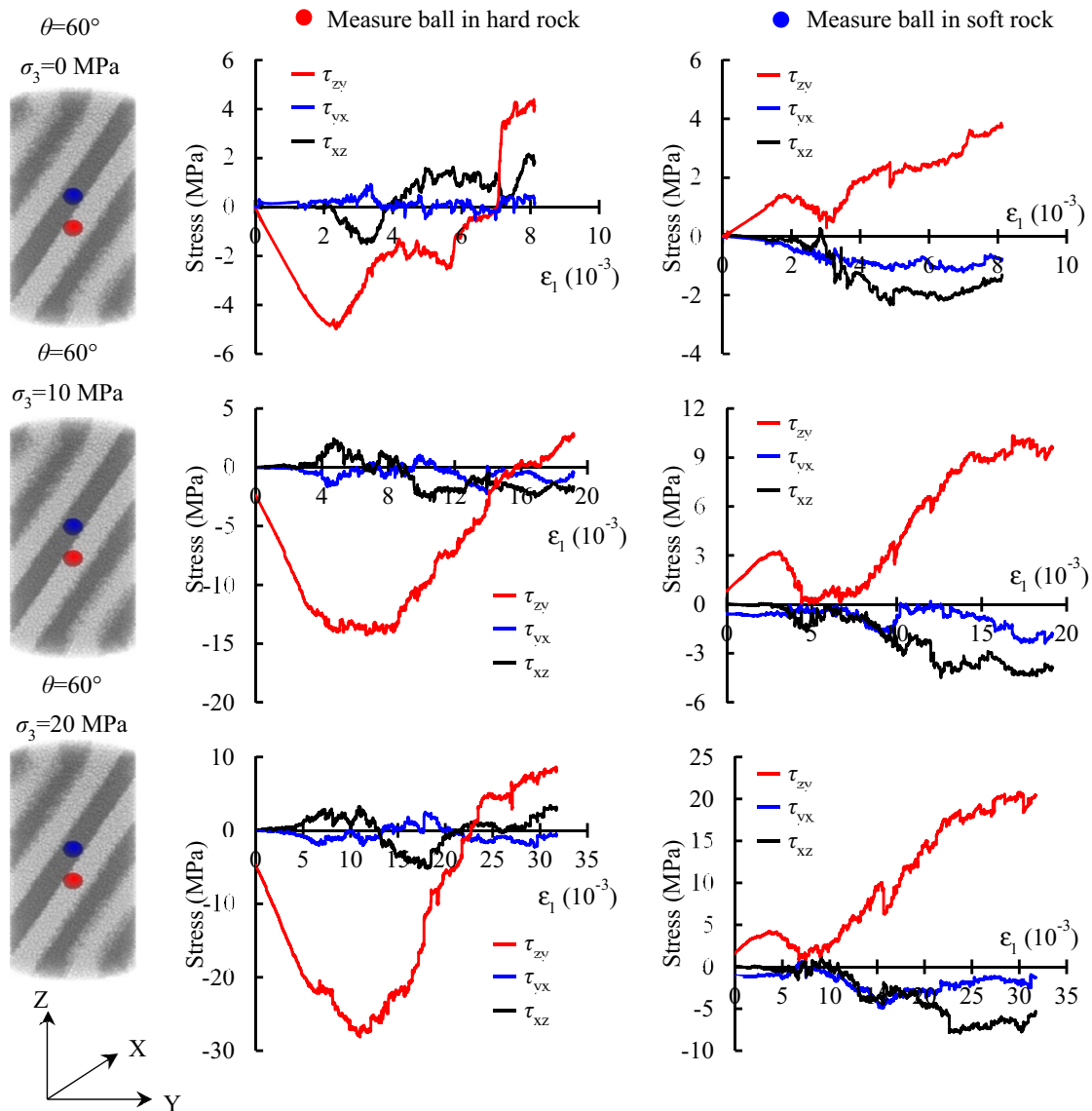


Fig. 20 Comparison of tangential stress variation between soft and hard particles of the model with θ_{60° bedding inclination under different confining pressures

resulting in multiple internal cracks and defects, where understanding these natural defects is sometimes more important than even recognizing the stress state after it has been formed. Shen et al. (2021). analyzed the probability of failure of interstratified slopes with consideration of rock damage and anisotropy of mechanical parameters. He concluded that the probability of failure of different slopes is dispersed; however along with the relaxation of mechanical parameters, the dispersion will decrease and the probability of failure will increase significantly for the shoulders, toes and weak layers of compliant slopes, but that the reverse slope remains relatively stable and undisturbed (Fig. 21b).

In Sect. 4, we analyzed the internal crack evolution and location of cracks in composite rock specimens at low confining pressures (0 MPa and 5 MPa), which indirectly reflected how the stresses during geological activity impact the internal damage of laminated slopes on the earth's surface, and also how the slopes are subsequently damaged when subjected to external stresses. Figure 10a and Fig. 10b indicates that the damage mainly occurs in the weak bedding and soft rock which was in agreement with Shen's conclusion. Besides, from the results of composite rock specimens with laminar dips of θ_{30° to θ_{75° , we can deduce that the downward slope will eventually slip

Fig. 21 Classification of stratified slopes. **a** A downward layered rock slope; **b** An anti-dip interbedded rock slope (Shen et al. 2021); **c** A vertical stratified rock slope

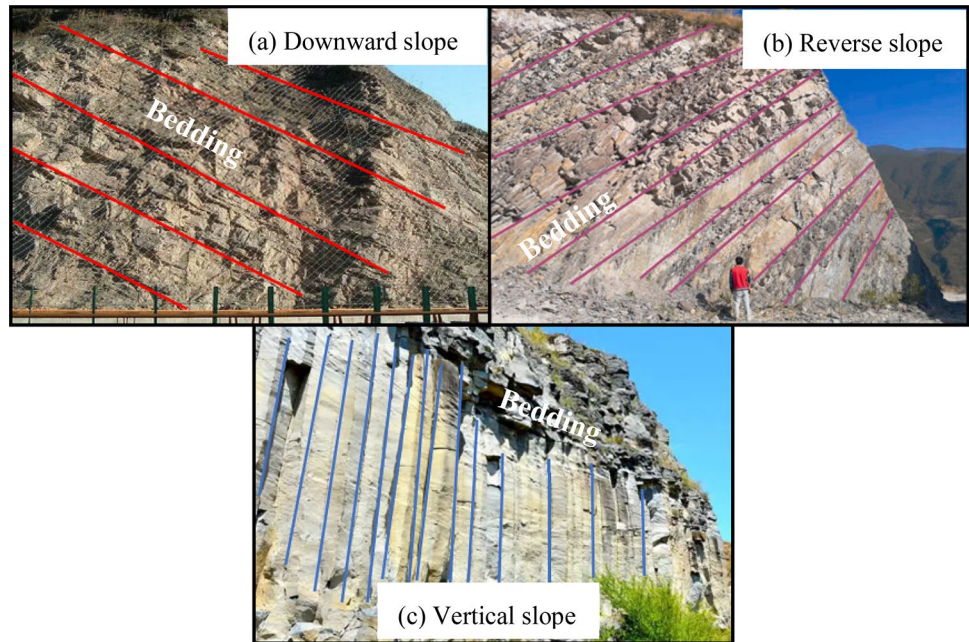
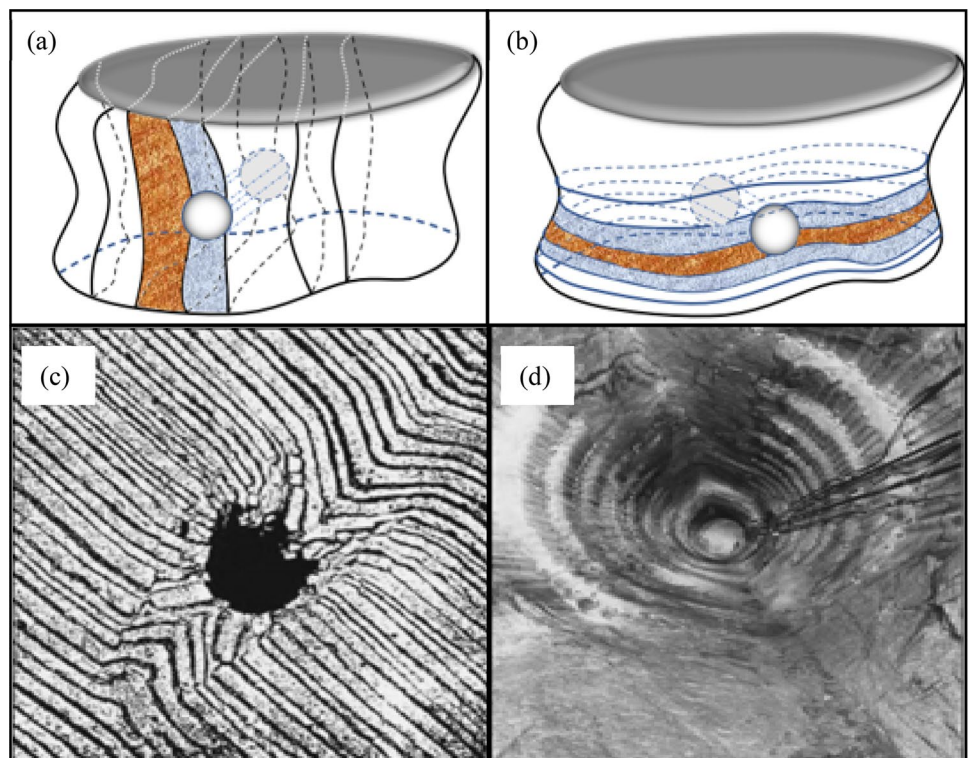


Fig. 22 Circular holes in laminated rock formations. **a** Tunnel scenario in a horizontally laminated rock mass; **b** Tunnel scenario in inclined laminated rock mass; **c** Wellbore breakdown through steeply inclined thin layers (Zhang 2013); **d** An experimental tunnel designed parallel to the intermediate principal stress direction in Canada (Read et al. 1998)



along the intermediate weak side when the slope is under great pressure at the top. Figure 16 displays the cracking process in a composite rock specimen at an inclination of θ_{60° , where we can derive that in the initial stress state (corresponding to early geological activity) the internal cracking of the laminated rock slope occurs mainly at

the layered face, which may increase the permeability of the laminated slope and reduce its mechanical strength, while as the stress continues to increase (corresponding to anthropogenic activities), the internal damage of the interbedded rock slope emerges preferentially in the soft rock and shows in some penetration tensile damage.

6.2 Implications for Stability of Composite Rock Strata in a Tunnel

Read et al. (1998) pointed out that the stability of an underground opening cannot be evaluated simply by satisfying the condition that the peak tangential stress at the edge of the opening remains below an unknown compressive strength of the rock blocks, a *in situ* mine-by test tunnel experiment was conducted which showing a bad-deformed V-shape by controlling the direction of maximum and minimum principal stress in the tunnel to maximum the damage possibility (shown in Fig. 22d). Then, he put forward some suggestions on tunnel design based on the experimental phenomena.

However, the influence of the soft and hard interlaced strata on the tunnel was ignored. In this paper, we investigated the condition of inner stress in hard and soft rock matrix, respectively, in Sect. 5, which can be an important guide to the stability of tunnels in deep composite rock formations. Figs. 17, 18, 19, 20 indicate that the internal stresses in the composite rock samples vary considerably at different inclination angles, and are mainly reflected in the tangential stresses. The internal stresses in the specimens with θ_0° bedding angle seem to be dominated by τ_{xz} in both soft and hard rocks, and it had the greatest undulation, but in the θ_{45° specimens τ_{zy} also reflected the destruction process of the rock samples in addition to τ_{xz} . The specimens in θ_{90° differed from the previous two in that their internal tangential stresses were most sensitive to τ_{xz} in hard rocks and τ_{zy} in soft rocks. Besides, the effect of the confining pressure on the internal stresses was only in terms of numerical magnitude and had no effect on the overall pattern, which was similar to the stress–strain curve of the test results. Combining the above symptoms, this paper proposes the following recommendations for the design and support of tunnels with composite rock formations. On the one hand, for the design of laminated rock formations with an inclination of θ_0° (as shown in Fig. 22b), priority should be given to the strength–deformation characteristics of soft rock, especially the influence of σ_z and τ_{xz} on soft rock matrix. On the other hand, for the inclined composite rock formation (shown in Fig. 22a), the influence of the weak structural surface is crucial; while the changes of τ_{xy} and τ_{xz} should be given priority in monitoring to prevent misalignment and damage. Figure 22c illustrates the damage pattern of a circular wellbore excavated in a laminated rock formation (Zhang 2013).

7 Conclusions

A series of three-dimensional discrete particle models of composite transversely isotropic rock were established to investigate the mechanical properties, internal cracking

behavior and the inner stress state between soft and hard rock. The headline findings are summarized as below:

- (1) Confining pressure and the inclination of the laminae have a significant regular effect on the peak strength of composite rock-like materials, showing a “U”-shaped variation with the increasing bedding dip angles and satisfying the Mohr’s law under varies confining pressure. Macroscopic damage modes fall into three main categories: tension–shear damage originating from soft rock, slip damage, and splitting damage originating from laminated surfaces. While as the confining pressure increases to 20 MPa, all specimens show the typical shear damage pattern.
- (2) Comparison with X-ray CT images indicates that the 3D model achieves satisfactory performance for internal cracking under triaxial compression simulation. On the one hand, the failure of internal matrix is dominated by the tensile cracking and mainly distributes in soft rock in the composite specimens with inclination angel of θ_0° and θ_{90° , and the other models present slip-shear failure along with the weak bedding faces, which is in agreement with the Jaeger’s theory. On the other hand, the dispersion of the cracks grows and the fractures convert to shear cracking behavior with increasing confining pressure, confining pressure enables to diminish the difference in mechanical behavior between the two types of rocks. The analysis of the crack evolution process shows that the cracks appear mainly at the weak surface at the beginning of the stress loading, and the rock matrix gets damaged and destroyed gradually as the stress increases in the specimens with bedding angle of θ_{30° to θ_{75° . However, the cracks emerge first in soft rock and then extent to hard rock when the bedding inclination is θ_0° and θ_{90° .
- (3) The analysis of the internal stress state displays a general agreement between the maximum principal stresses and the stress–strain diagrams for both the soft rock and the hard rock. However, the maximum principal stresses in the hard rock are significantly higher than in the soft rock in the specimens of θ_0° and θ_{90° laminar dip; while the situation is reversed in the specimens with θ_{45° and θ_{60° bedding angle. Besides, the stress gap between soft and hard rocks is dominated further by tangential stresses: τ_{xz} and τ_{zy} are the predominant factor in the destruction of rocks matrix, but τ_{yx} has the minimal influence.

Acknowledgements This research was supported by the National Natural Science Foundation of China (42077231) and the Fundamental Research Funds for the Central Universities (2021ZDPYJQ002).

Data availability The data used to support the findings of this study are available from the corresponding author upon request.

Declarations

Conflict of interest The authors declare that they have no conflict of interests.

References

- Ademović N, Kurtović A (2021) Influence of planes of anisotropy on physical and mechanical properties of freshwater limestone (mudstone). *Constr Build Mater* 268:121174
- Cao WK, Liu W (2022) The wellbore stability study in bedding shale formation the condition of plasticity. *Chem Technol Fuels Oils* 58:220–231
- Chen DH, Chen H, Zhang W (2022) An analytical solution of equivalent elastic modulus considering confining stress and its variables sensitivity analysis for fractured rock masses. *J Rock Mech Geotech Eng* 14:825–836
- Cheng JL, Yang SQ, Chen K (2017) Uniaxial experimental study of the acoustic emission and deformation behavior of composite rock based on 3D digital image correlation (DIC). *Acta Mech Sin* 33(6):999–1021
- Cheng JL, Yang SQ, Yin PF (2018) Experimental study of the deformation and strength behavior of composite rock specimens in unloading confining pressure test. *J China Univ Min Technol* 47:6
- Cheng JL, Luo S, Li JB (2020) Triaxial loading test of strength behavior and failure mechanism of composite rock. *J Min Safety Eng* 37:6
- Chiu CC, Wang TT, Weng MC (2013) Modeling the anisotropic behavior of jointed rock mass using a modified smooth-joint model. *Int J Rock Mech Min Sci* 62:14–22
- Cho JW, Kim H, Jeon S (2012) Deformation and strength anisotropy of *Asan gneiss, Boryeong shale*, and *Yeoncheon schist*. *Int J Rock Mech Min Sci* 50:158–169
- Deng PH, Liu QS, Huang X (2022) FDEM numerical modeling of failure mechanisms of anisotropic rock masses around deep tunnels. *Comput Geotech* 142:104535
- Ding XB, Zhang LY, Zhu HH (2014) Effect of model scale and particle size distribution on PFC3D simulation results. *Rock Mech Rock Eng* 47:2139–2156
- Dobróka M, Szabó NP, Dobróka TE (2022) Multi-exponential model to describe pressure-dependent P- and S-wave velocities and its use to estimate the crack aspect ratio. *J Rock Mech Geotech Eng* 14:385–395
- Dong ZJ, Yang SQ, Sun BW (2022) Three-dimensional grain-based model study on triaxial mechanical behavior and fracturing mechanism of granite containing a single fissure. *Theoret Appl Fract Mech* 122:103602
- Duan K, Kwok CY (2016) Evolution of Stress-induced borehole breakout in inherently anisotropic rock: insights from discrete element modeling. *J Geophys Res* 121:2361–2381
- Duan K, Kwok CY, Pierce M (2016) Discrete element method modeling of inherently anisotropic rocks under uniaxial compression loading. *Int J Numer Anal Meth Geomech* 40:1150–1183
- Ghazvinian A, Vaneghi RG, Hadei MR (2013) Shear behavior of inherently anisotropic rocks. *Int J Rock Mech Min Sci* 61:96–110
- He JM, Afolagboye LO (2018) Influence of layered orientation and interlayer bonding force on the mechanical behavior of shale under Brazilian test conditions. *Acta Mechanica Sinica* 34(2):349–358
- He R, Ren L, Zhang R (2022) Anisotropy characterization of the elasticity and energy flow of Longmaxi shale under uniaxial compression. *Energy Rep* 8:1410–1424
- Hill R (1950) *The mathematical theory of plasticity*. Oxford University Press, Oxford
- Ivars DM, Pierce ME, Darcel C (2011) The synthetic rock mass approach for jointed rock mass modeling. *Int J of Rock Mech Min Sci* 48:219–24
- Jeager JC (1960) Shear failure of transversely isotropic rock. *Geol Mag* 97:65–72
- Jiang MJ, Yan HB, Zhu HH (2011) Modeling shear behavior and strain localization in cemented sands by two-dimensional distinct element method analyses. *Comput Geotech* 38:14–29
- Lee H, Jeon S (2011) An experimental and numerical study of fracture coalescence in pre-cracked specimens under uniaxial compression. *Int J Solids Struct* 48:979–999
- Liu LW, Li HB, Chen SH (2021) Effects of bedding planes on mechanical characteristics and crack evolution of rocks containing a single pre-existing flaw. *Eng Geol* 293:106325
- Mehranpour MH, Kulatilake PHSW (2017) Improvements for the smooth joint contact model of the particle flow code and its applications. *Comput Geotech* 87:163–177
- Park B, Min KB (2015) Bonded-particle discrete element modeling of mechanical behavior of transversely isotropic rock. *Int J Rock Mech Min Sci* 76:243–255
- Park B, Min KB, Thompson N (2018) Three-dimensional bonded-particle discrete element modeling of mechanical behavior of transversely isotropic rock. *Int J Rock Mech Min Sci* 110:120–132
- Potyondy D O., 2012, Flat-Jointed Bonded-Particle Material for Hard Rock. American Rock Mechanics Association
- Potyondy DO (2015) The bonded-particle model as a tool for rock mechanics research and application: current trends and fracture directions. *Geosyst Eng* 18(1):1–28
- Potyondy DO, Cundall PA (2004) A Bonded-particle model for rock. *Int J Rock Mech Min Sci* 41(8):1329–1364
- Read RS, Chandler NA, Dzik EJ (1998) In situ strength criteria for tunnel design in highly-stressed rock masses. *Int J Rock Mech Min Sci* 35:261–278
- Roy DG, Singh TN (2015) Effect of heat treatment and layer orientation on the tensile strength of a crystalline rock under Brazilian test condition. *Rock Mech Rock Eng* 49(5):1663–1677
- Saeidi O, Vaneghi RG, Rasouli V (2013) A modified empirical criterion for strength of transversely anisotropic rocks with metamorphic origin. *Bull Eng Geol Env* 72(2):257–269
- Saeidi O, Rasouli V, Vaneghi RG (2014) A modified failure criterion for transversely isotropic rocks. *Geosci Front* 5:215–225
- Sapari NK, Zabidi H (2019) Determination of strength variation in jointed anisotropic rocks behavior using UCS and Brazilian tensile test. *Mater Today Proc* 17:905–911
- Shen PW, Tang HM, Zhang B (2021) Investigation on the fracture and mechanical behaviors of simulated transversely isotropic rock made of two interbedded materials. *Eng Geol* 286:106058
- Shi XC, Yang X, Meng YF (2016) An anisotropic strength model for layered rocks considering planes of weakness. *Rock Mech Rock Eng* 49(9):3783–3792
- Singh M, Samadhiya NK, Kumar A (2015) A nonlinear criterion for triaxial strength of inherently anisotropic rocks. *Rock Mech Rock Eng* 48(4):1387–1405
- Sun BW, Yang SQ, Xu J (2022) Discrete element simulation on failure mechanical behavior of transversely isotropic shale under two kinds of unloading paths. *Theoret Appl Fract Mech* 121:103466

- Tien YM, Tsao PF (2000) Preparation and mechanical properties of artificial transversely isotropic rock. *Int J Rock Mech Min Sci* 37:1001–1012
- Tsai SW, Wu E (1971) A general theory of strength of anisotropic materials. *J Compos Mater* 5:58
- Valente S, Fidelibus C, Loew S (2012) Analysis of fracture mechanics tests on opalinus clay. *Rock Mech Rock Eng* 45(5):767–779
- Vervoort A, Min KB, Konietzky H (2014) Failure of transversely isotropic rock under Brazilian test conditions. *Int J Rock Mech Min Sci* 70:343–352
- Wang J, Xie LZ, Xie HP (2016) Effect of layer orientation on acoustic emission characteristics of anisotropic shale in Brazilian tests. *J Nat Gas Sci Eng* 36:1120–1129
- Wang ZH, Wang M, Zhou L (2022) Research on uniaxial compression strength and failure properties of stratified rock mass. *Theoret Appl Fract Mech* 121:103499
- Weng MC, Wu PL, Fang CH (2022) Evaluating the effect of anisotropy on hydraulic stimulation in a slate geothermal reservoir. *Rock Mech Rock Eng*. <https://doi.org/10.1007/s00603-022-03020-5>
- Yang SQ, Yin PF, Huang YH (2019a) Experiment and discrete element modeling on strength, deformation and failure behavior of shale under brazilian compression. *Rock Mech Rock Eng* 52(11):4339–4359
- Yang SQ, Yin PF, Huang YH (2019b) Strength, deformability and X-ray micro-CT observations of transversely isotropic composite rock under different confining pressures. *Eng Fract Mech* 214:1–20
- Yang SQ, Yin PF, Li B (2020) Behavior of transversely isotropic shale observed in triaxial tests and Brazilian disc tests. *Int J Rock Mech Min Sci* 133:104435
- Yin PF, Yang SQ (2018) Experimental investigation of the strength and failure behavior of layered sandstone under uniaxial compression and Brazilian testing. *Acta Geophys* 66(4):585–605
- Yin PF, Yang SQ, Tian WL (2019) Discrete element simulation on failure mechanical behavior of transversely isotropic rocks under different confining pressure. *Arab J Geosci*. <https://doi.org/10.1007/s12517-019-4807-0>
- Zhang JC (2013) Borehole stability analysis accounting for anisotropies in drilling to weak bedding planes. *Int J Rock Mech Min Sci* 60:160–170
- Zhang YL, Shao JF, Saxcé GD (2019) Study of deformation and failure in an anisotropic rock with a three-dimensional discrete element model. *Int J Rock Mech Min Sci* 120:17–28

Publisher's Note Springer Nature remains neutral with regard to jurisdictional claims in published maps and institutional affiliations.

Springer Nature or its licensor (e.g. a society or other partner) holds exclusive rights to this article under a publishing agreement with the author(s) or other rightsholder(s); author self-archiving of the accepted manuscript version of this article is solely governed by the terms of such publishing agreement and applicable law.